Kinetic Model Development and Bayesian Uncertainty Quantification for the Complete Reduction of Fe-based Oxygen Carriers with CH_4, CO, and H_2 for Chemical Looping Combustion

Anca Ostace[a], Yu-Yen Chen[b], Robert Parker[c], David S. Mebane[d], Chinedu Okoli[e,f], Andrew Lee[e,f], Andrew Tong[b], Liang-Shih Fan[b], Lorenz T. Biegler[c], Anthony P. Burgard[e], David C. Miller[e], Debangsu Bhattacharyya[a*]

[a] *Department of Chemical and Biomedical Engineering, West Virginia University, 401 Evansdale Drive, Morgantown, WV 26506, USA*
[b] *William G. Lowrie Department of Chemical and Biomolecular Engineering, 151 West Woodruff Avenue, Koffolt Laboratories, The Ohio State University, Columbus, OH 43210, USA*
[c] *Department of Chemical Engineering, Carnegie Mellon University, Pittsburgh, PA 15213, USA*
[d] *Department of Mechanical and Aerospace Engineering, West Virginia University, Morgantown, WV 26506, USA*
[e] *National Energy Technology Laboratory, 626 Cochrans Mill Road, Pittsburgh, PA 15236, USA*
[f] *NETL Support Contractor, 626 Cochrans Mill Road, Pittsburgh, PA 15236, USA*

Abstract

Three kinetic models are developed and calibrated for the complete multi-step reduction of an Fe-based oxygen carrier (OC) particle with CH_4, CO, and H_2, using data from thermogravimetric analysis. The complete reduction rate profiles exhibit complex dynamics whose trajectory is significantly different depending on the reducing gas. A Bayesian model building and parameter estimation framework is applied for simultaneous parameter and model structure uncertainty quantification. The final models show excellent agreement between model predictions and calibration data, as well as new data not used for calibration (for the reduction of the OC with CH_4). Parameter uncertainty is quantified by determining joint posterior distribution, and model structure uncertainty is addressed by incorporating Gaussian process stochastic functions (represented by Bayesian smoothing splines) into the kinetic models. The final kinetic models with discrepancy functions are readily employable in equation-oriented simulation and optimization platforms.

Key Words

Uncertainty quantification; model structure uncertainty; parameter uncertainty; Bayesian calibration; Bayesian model building; chemical looping; oxygen carrier

* Corresponding author.
Tel:1-304-293-9335, E-mail: Debangsu.Bhattacharyya@mail.wvu.edu

1 Introduction

Chemical looping combustion (CLC) technology, first developed in 1954 (Lewis and Gilliland, 1954), has garnered renewed interest in recent years because of its inherent carbon dioxide capture capability. Innovative CLC applications open up possibilities for converting various carbonaceous fuels (methane, coal, and biomass) into power, syngas, and chemicals in novel, efficient, and clean ways (Yu et al., 2019). The great advantage of oxygen carriers (OCs) is that as the metal oxide particles transfer O_2 from combustion air to fuel, direct contact between air and fuel is avoided. Thus, the gas streams exiting CLC reactors are CO_2 and H_2O streams and an O_2-depleted air stream. This combustion technology with inherent carbon capture helps avoid the high cost of an air separation unit necessary in traditional oxy-combustion technologies and the high CO_2 capture cost often imposed by post-combustion capture technologies. CLC consists of two or three interconnected reactors and relies on the cyclic redox reactions of circulating metal oxides that act as OCs. The OCs provide the necessary amount of oxygen for hydrocarbon conversion during the reduction step of CLC, while during oxidation, the depleted OCs are replenished with molecular oxygen from air, releasing heat (Cheng et al., 2018).

Subject to extensive research, the development of OCs is a challenging topic due to the complex reaction mechanism in chemical looping redox reactions. Among the many different OCs developed to date, iron-based OCs stand out as versatile, cost-effective, and environment friendly materials with high oxygen-carrying capacity. The $Fe_2O_3 \rightarrow Fe_3O_4 \rightarrow FeO \rightarrow Fe$ stepwise reduction of iron-based OCs makes them suitable for various chemical looping applications such as power generation and syngas and hydrogen production. The stepwise reduction/multiple oxidation states of iron-based OCs have proven to be very advantageous in moving bed reactor systems extensively studied at the Clean Energy Research Laboratory at the Ohio State University (OSU) for different applications for the full and partial oxidation of carbonaceous fuels (Hsieh et al., 2018; Park et al., 2020; Sridhar et al., 2012; Tong et al., 2014, 2013). Counter-current moving bed reactors are particularly well-suited to exploit the high oxygen transport capacity of iron oxide, as the equilibrium limitation on iron oxide reduction is removed in the moving bed solid-gas contacting configurations (Tong et al., 2018; Yu et al., 2019), and high extent of reduction of the OC can be achieved along with practically complete fuel conversion to CO_2 and H_2O (Hsieh et al., 2018; Kathe et al., 2016; Nadgouda et al., 2017). Achieving high solids conversion ensures more oxygen transfer from the OC per unit of fuel. This, in turn, means a lower solids circulation rate and lower costs, improving the efficiency of the system (Kathe et al., 2016). Previous studies limited the reduction of Fe_2O_3 to Fe_3O_4 (Abad et al., 2007a; Luo et al., 2014; Zhang et al., 2018) or FeO (Su et al., 2017). This is due to thermodynamic limitations and poor reactivity associated with complete reduction that could lead to decreased fuel conversions and CO_2 purity in processes carried out in fluidized beds (Luo et al., 2014;

Zhang et al., 2018), the type of reactor most often encountered in CLC applications. In this study, the development of kinetic models for the full reduction of OSU's Fe-based OC with CH_4, CO, and H_2 is presented, addressing a critical need for models that can be used to predict the composition of the OC with the progression of the reaction all the way to the complete reduction of the Fe-based OC. These kinetic models enable the modeling of CLC processes that rely on moving bed reactors, where the near complete reduction of Fe-based OCs is desirable and advantageous. However, they can be used to model any CLC process.

The development of a new generation of advanced computational tools (Lee et al., 2021) for the optimization of multi-scale chemical processes can enable the accelerated development and scale up of CLC technologies in a significant way through design of experiments and rigorous optimization for design and operation (Miller et al., 2011; Syamlal et al., 2011). Such tools rely on predictive, accurate mathematical models for reliable results. Additionally, control, fault detection, and predictive maintenance applications also depend on adequate models. Thus, the development of predictive mathematical models is a critical component in the advancement of new technologies like CLC. Furthermore, quantifying the uncertainty inherent to mathematical models can be very helpful for process design and optimization, reducing scale-up risks and improving predictive performance uncertainty for reactor design.

In general, mathematical models of reactors and processes comprise tightly coupled sub-models that represent physical and thermodynamic properties, reactions, mass and heat transfer, and other aspects of the modeled process. The accuracy and reliability of these sub-models are imperative for the predictive capability of the unit and process models. In the case of CLC, the reaction sub-models consist of the kinetics of the OC reduction reactions, which can vary widely depending on the reducing fuel and metal oxide, preparation method, and conditions and duration of testing (Abad et al., 2007b; Adánez et al., 2004; García-Labiano et al., 2004; Han, 2016; Han et al., 2014). In this study, our previously presented Bayesian model building and parameter estimation framework for CO_2 adsorption applications (Ostace et al., 2019) is extended and applied to the development of predictive kinetic models for the complete reduction of an OSU iron-based OC with the main gaseous fuels encountered in CLC applications (CH_4, CO, and H_2) based on experimental data collected using thermogravimetric analyzers (TGA). While numerous studies have examined the performance of Fe-based OCs over their first reduction step, studies that examine their complete reduction and model the change in each of their oxidation states are extremely scarce. The models built using this framework are suitable for uncertainty quantification studies, as the estimates of model parameters are probability density functions that are the measure of uncertainty in the parameters. In addition to parameter uncertainty, the Bayesian framework outlines an efficient way for the simultaneous quantification of model structure uncertainty using Bayesian Smoothing Spline ANalysis Of VAriance (BSS-ANOVA) Gaussian Process (GP) which is then built into the kinetic models, also referred to as

discrepancy reduced modeling (DDRM) (Li et al., 2017). Including the quantified model structure uncertainty in the form of discrepancy functions in the kinetic models (intrusive uncertainty quantification) results in better-fitting models without a corresponding increase in computational expense associated with their use. The final models are a combination of mechanistic models and stochastic discrepancy functions, retaining important features of their first-principles model structure while incorporating information based on the experimental data. The kinetic models with intrusive uncertainty are suitable for use in equation-oriented optimization frameworks relying on numerical solvers, as they are twice continuously differentiable. To the best of our knowledge, there is no study in the scientific literature for modeling and Bayesian calibration of the reduction of Fe-based OCs over their complete conversion range, quantifying parameter and model structure uncertainty simultaneously.

The approach for quantifying model structure uncertainty and building it into the model, and using Bayesian calibration to estimate the posterior distributions of the parameters, has been successfully applied to a number of applications. It was used to develop a continuum model that replicates defect concentration profiles near grain boundaries in calcium-doped ceria as measured by electron-energy loss spectroscopy in an aberration-corrected scanning transmission electron microscope (Tong et al., 2020). Also, a high-fidelity reduced-order coarsening model was developed for microstructure evolution in the electrodes of solid oxide fuel cells (Lei et al., 2019). Bayesian calibration has also been demonstrated in carbon capture studies (Bhat et al., 2017; Li et al., 2017; Ostace et al., 2019) applied to build accurate predictive adsorption sub-models with quantified uncertainty and to propagate the uncertainty through process-scale reactor models.

This paper is arranged as follows. The experimental procedure, data, and data processing approach are presented first. Then the Bayesian model building and parameter estimation framework is presented, describing in detail each component of the Bayesian framework. Finally, the results—best-fitting kinetic models, their parameter distributions, model predictions vs. experimental data, and model validation—are presented. We close with a discussion on how the calibrated kinetic models can be implemented and used in a process model for uncertainty propagation, or simply for prediction using a point estimate from the parameter distribution, for optimization and control studies.

Key contributions presented in this paper are:

- The development of a Bayesian model building and parameter estimation framework for CLC systems/applications.
- The development of dynamic kinetic models for the full reduction of an Fe-based OC with CH_4, CO, and H_2 with the ability to predict the composition of the OC with the progression of the reaction, suitable for use in stochastic and deterministic studies.
- Simultaneous quantification of the uncertainty in model parameters and model structure.
- Full posterior probability distribution of model parameters.

- Parameter point estimates and 95 % credible intervals of model parameters in tabular form.

2 Reduction Experiments

2.1 Materials and Experimental Procedure

The OC material used in this study is a mixture of iron and titanium oxides, which has shown a robust recyclability over multiple redox cycles and the ability to generate high purity syngas through partial oxidation (Chen et al., 2020). The OC particles are prepared by mechanically mixing the Fe_2O_3 (Noah Tech, 99.9%+ purity) and TiO_2 powders (Noah Tech, 99.9%+ purity) and forming them into 1.5 mm spherical particles in a ball mill, followed by a calcination in air at 950°C for six hours. The synthesized OC particles are composed of Fe_2TiO_5 (pseudobrookite) and TiO_2 (rutile) phases, with apparent and true particle densities of 2510 kg/m^3 and 4310 kg/m^3, respectively, with a particle porosity of 0.42. For a detailed characterization of the OC particles, readers are directed to previous work by Chen et al. (Chen et al., 2020).

The reduction kinetics of the OC particles are investigated via thermogravimetric analysis (Setaram Setsys Evolution 1750) experiments under atmospheric pressure and isothermal conditions. Experiments cover a typical-for-CLC range of different temperatures (800–1000°C) and reactant gas concentrations (10–50 % CH_4, CO, or H_2). For each experimental scenario, only one fully oxidized particle is loaded in the quartz crucible of the TGA balance. The sample is dried under N_2 flow at 200°C for 15 minutes before being heated to the desired test temperature. The mass flow of the reactant (CH_4, CO, or H_2) and carrier (N_2) gases into the TGA setup is controlled using an Alicat mass flow controller. The total gas flowrate for all the experiments conducted in this study is fixed at 248 mL/min, measured at normal conditions of temperature and pressure (20°C, 1 atm).

2.2 Data Processing and Observations

During the experiment, the sample weight, m_{OC} [mg], is recorded as a function of time. Then, based on the amount of oxygen lost ($m_{oxi} - m_{red}$), the overall conversion fraction X is calculated as:

$$X = \frac{m_{oxi} - m_{OC}}{m_{oxi} - m_{red}} \tag{1}$$

Here, X [-] is the overall OC conversion (or extent of reduction), and m_{oxi} [mg] and m_{red} [mg] are the weights of the fully oxidized and reduced samples, respectively. In this study, the reduction experiments are conducted under conditions that ensured that the OC was fully reduced. Thus, in computing the overall conversion of the OC (Eq. (1)), the initial weight m_{oxi} is the weight of Fe_2O_3, and the final weight m_{red} that of Fe. Given that X is defined based on the amount of oxygen removed from Fe_2O_3, reduction of the

OC to Fe_3O_4 corresponds to 11 % oxygen loss (or 11 % X), reduction to FeO corresponds to 33% X, and reduction to Fe corresponds to 100 % X.

It should be noted that at the high temperatures relevant to CLC, iron carbide (Fe_3C) formation is a prevalent issue in the reduction of iron ore with carbonaceous fuels (Campos et al., 2013; Nasr and Plucknett, 2014). Because carbon deposition was observed in our reduction with CH_4 and CO TGA measurements, the overall conversion curves were truncated at the point where the conversion started decreasing (at approximately 90 % conversion for the reduction of the OC with CH_4).

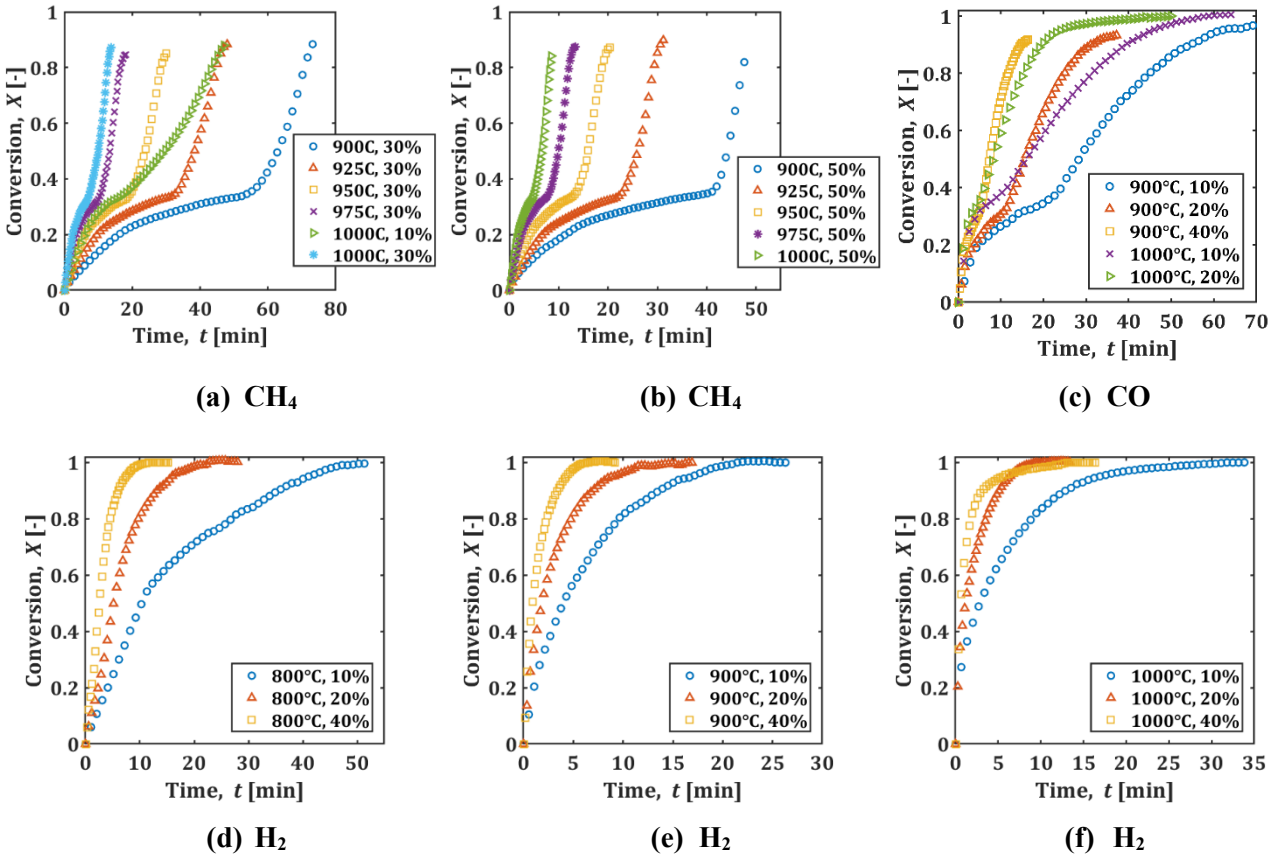

(a) CH_4 **(b) CH_4** **(c) CO**

(d) H_2 **(e) H_2** **(f) H_2**

Figure 1. Reduction conversion curves of the Fe-based OC particle at various temperatures and reacting gas concentrations in TGA. Only 50 data points are shown at each operating condition for legibility.

The TGA results are shown in Figure 1. Figures 1 (a) and (b) show the reduction conversion curves of the OC particle with CH_4. Figure 1 (c) shows the reduction conversion curves of the OC particle with CO, and Figures 1 (d), (e), and (f) show the reduction conversion curves of the OC particle with H_2. An important observation is that the overall reduction conversion profiles of the OC are highly dependent on reacting gas and operating conditions (reacting gas concentration, temperature). Furthermore, the conversion profiles obtained from the reduction with carbonaceous fuel (i.e., CH_4 and CO) exhibit a notable trend: the initially fast reduction rate decreases, reaching a plateau when X is approximately 33 %, and then it accelerates

again after X exceeds 33 %. Thus, the reduction takes place in a two-stage mechanism, with the first stage having a lower reduction rate than the second. This behavior has been previously reported and is related to the reduction state of the OC (Campos et al., 2013; Miller and Siriwardane, 2013; Nasr and Plucknett, 2014). However, the kinetic modeling of this behavior is challenging, and to the best of the author's knowledge, a model capable of emulating the reaction rate switch such as the one observed in the reduction of iron-based OCs with hydrocarbons has not yet been reported.

3 Framework for Model Building and Uncertainty Quantification

The first step of our model building framework is to develop kinetic models that describe the reaction mechanism of each solid-gas reacting pair. These models serve as the base models in our Bayesian model building framework. Once adequate base models have been developed, the next step is parameter estimation (or parameter uncertainty quantification), where the posterior probability distributions of the model parameters are obtained. Model structure inadequacy is addressed by inserting GP discrepancy functions into our base models, effectively creating hybrid stochastic models comprised of the mechanistic base models and the stochastic data-driven discrepancy functions. Each new model proposal is followed by another parameter estimation step. After having postulated the base models and the discrepancy-augmented hybrid models and estimating their parameters (the uncertainty in their parameters quantified), the final step is to identify the most adequate model via model selection.

The most adequate models will inherently contain a measure of the error in the mechanistic models with respect to the experimental data in the form of the BSS-ANOVA GP discrepancy functions. Inserting the GP discrepancy functions into the base models effectively means correcting the model predictions such that the experimental data are reproduced to within the estimated observation error (Mebane et al., 2013). The final stochastic kinetic models are written in a form that can be readily used in process models, effectively propagating the kinetic uncertainties to the unit or process models. Additionally, representative point estimates of the model parameters are provided to facilitate the use of the models only in their predictive capacity when the propagation of the uncertainty is not of interest.

The model building method outlined here and summarized in Table 1 is a systematic, sequential, and tractable approach, where the complexities of the reactions that are not captured by the base kinetics are *measured* and accounted for by discrepancy functions whose terms describe more complexity with each model proposal iteration.

Table 1. Bayesian model building framework and uncertainty quantification.

Step 1:	Propose base kinetic model based on existing reaction mechanisms for solid-gas reactions (Table 2) identified using a modified Hancock and Sharp (Hancock and Sharp, 1972) method (refer to section 4). Stage I: Identify rate controlling reaction mechanism(s) and corresponding model(s). Stage II: Formulate the dynamic kinetic model. Estimate the kinetic model parameter distributions by sampling from the prior distributions using Markov Chain Monte Carlo (MCMC) methods (refer to section 5.1).
Step 2:	Propose new hybrid models by inserting discrepancy functions with sequentially increasing number of terms into the base model (refer to section 5.2 and 5.3) and estimate the parameter distribution using MCMC for each new hybrid model.
Step 3:	Select the most adequate model by means of Bayesian model comparison using the Bayesian Information Criterion (BIC) (refer to section 5.4).

4 Development of the Base Kinetic Model / Framework for Base Kinetic Model Development

Hancock and Sharp (Hancock and Sharp, 1972) presented a method for comparing isothermal solid-state reaction kinetics based on the classical equation for analysis of nucleation and growth. The general rate of a solid-state reaction can be described as

$$\frac{\mathrm{d}X}{\mathrm{d}t} = kf(X) \tag{2}$$

where t [s] is time, $f(X)$ is the function that represents the reaction mechanism, and k [mol^{-n} m^{3n} s^{-1}] is the reaction rate constant given by the Arrhenius equation:

$$k = k_0 \exp\left(\frac{-E_a}{RT}\right) \tag{3}$$

Here, k_0 [mol^{-n} m^{3n} s^{-1}] is the pre-exponential factor (n [-] is the reaction order), E_a [kJ mol^{-1}] is the activation energy, R [kJ mol^{-1} K^{-1}] is the ideal gas constant, and T [K] is the temperature. Integrated, Eq. (2) becomes

$$g(X) = \int_0^X \frac{\mathrm{d}X}{\mathrm{d}t} = k(T)t \tag{4}$$

where $g(X)$ is the integral form of the reaction model.

In general, there are four groups of kinetic models with distinct reaction mechanisms for solid-gas reactions, classified according to their mechanistic basis: diffusion, geometrical contraction (or phase boundary-controlled), nucleation and nuclei growth models, and reaction order models. The differential ($f(X)$) and integral ($g(X)$) forms of these models are presented in Table 2 (Khawam and Flanagan, 2006).

Table 2. Solid-state rate and integral expressions for different reaction models (Khawam and Flanagan, 2006).

Mechanism	**Model**	m	**Differential Form** $f(X) = \frac{1}{k}\frac{dX}{dt}$	**Integral Form** $g(X) = kt$
Diffusion	1-D	0.62	$1/2X$	X^2
	2-D	0.57	$(-\ln(1-X))^{-1}$	$(1-X)\ln(1-X)+X$
	3-D (Jander)	0.54	$\frac{3}{2}(1-X)^{\frac{2}{3}}\left(1-(1-X)^{\frac{1}{3}}\right)$	$\left(1-(1-X)^{\frac{1}{3}}\right)^2$
	Ginstling-Brounshtein	0.57	$\frac{3}{2}\left((1-X)^{-\frac{1}{3}}-1\right)$	$1-\frac{2X}{3}-(1-X)^{\frac{2}{3}}$
Nucleation	Power law ($n=2$)		$2X^{\frac{1}{2}}$	$X^{\frac{1}{2}}$
	Power law ($n=3$)		$3X^{\frac{2}{3}}$	$X^{\frac{1}{3}}$
	Power law ($n=4$)		$4X^{\frac{3}{4}}$	$X^{\frac{1}{4}}$
	Avrami-Erofe'ev ($n=2$)	2	$2(1-X)(-\ln(1-X))^{\frac{1}{2}}$	$(-\ln(1-X))^{\frac{1}{2}}$
	Avrami-Erofe'ev ($n=3$)	3	$3(1-X)(-\ln(1-X))^{\frac{1}{3}}$	$(-\ln(1-X))^{\frac{1}{3}}$
	Avrami-Erofe'ev ($n=4$)		$4(1-X)(-\ln(1-X))^{\frac{1}{4}}$	$(-\ln(1-X))^{\frac{1}{4}}$
	Prout-Tompkins		$X(1-X)$	$\ln(X(1-X)^{-1})+C^{\dagger}$
Contraction	Contracting Area (2-D)	1.11	$2(1-X)^{\frac{1}{2}}$	$1-(1-X)^{\frac{1}{2}}$
	Contracting Volume (3-D)	1.07	$3(1-X)^{\frac{2}{3}}$	$1-(1-X)^{\frac{1}{3}}$
Reaction-order models	Zero-order	1.24	1	X
	First-order	1	$1-X$	$-\ln(1-X)$
	Second-order		$(1-X)^2$	$(1-X)^{-1}-1$
	Third-order		$(1-X)^3$	$0.5((1-X)^{-2})$

† Constant of integration.

Our base kinetic model development framework is divided in two main stages: identifying the reaction mechanisms that describe the reduction of the Fe-based OC with CH_4, CO, and H_2, and formulating a dynamic kinetic model to be used as the base model in the Bayesian calibration and model building framework.

Stage I. Reaction Mechanisms

The reduction reactions of the OC with the three gaseous fuels (CH_4, CO, H_2) under consideration are listed in Table 3.

Table 3. Reactions of the Fe-based OC with CH_4, CO, and H_2.

Initial Fe Oxidation State	CH_4 Reduction Reaction	CO Reduction Reaction	H_2 Reduction Reaction
III	$12Fe_2O_3 + CH_4 \rightarrow 8Fe_3O_4 + CO_2 + H_2O$	$3Fe_2O_3 + CO \rightarrow 2Fe_3O_4 + CO_2$	$3Fe_2O_3 + H_2 \rightarrow 2Fe_3O_4 + H_2O$
II, III	$4Fe_3O_4 + CH_4 \rightarrow 12FeO + CO_2 + H_2O$	$Fe_3O_4 + CO \rightarrow 3FeO + CO_2$	$Fe_3O_4 + H_2 \rightarrow 3FeO + H_2O$
II	$4FeO + CH_4 \rightarrow 4Fe + CO_2 + H_2O$	$FeO + CO \rightarrow Fe + CO_2$	$FeO + H_2 \rightarrow Fe + H_2O$

Based on the change in the Fe oxidation state and the reactions, the overall reduction process with each gas is considered a three-step reaction, where the first step is the reduction from Fe(III) to Fe(III,II) and accounts for 1/9 of the oxygen available to be consumed on the OC, the second is the reduction from Fe(III,II) to Fe(II), accounting for 2/9 of the oxygen, and the third is the reduction from Fe(II) to Fe, accounting for 2/3 of the oxygen. Based on the contribution of each reaction to the overall conversion, the first step in developing the base kinetic models is to divide the experimental data in three sections, as shown in Figure 2, for the reduction of the OC with 30 % CH_4 at 900 °C. Note that partitioning the data in this manner does not assume that the reactions proceed in series.

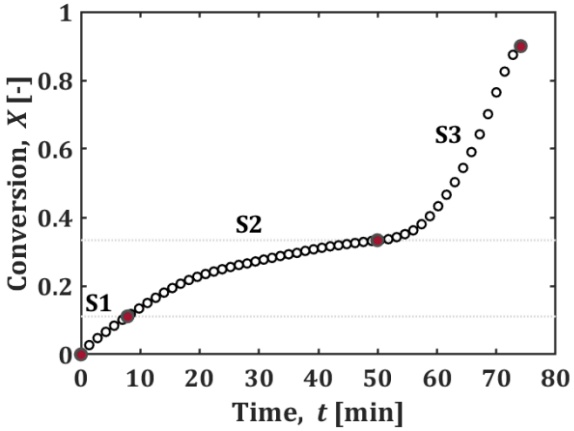

Figure 2. Reduction of the OC with 30 % CH_4 at 900 °C. Dividing overall conversion data based on each reaction steps' contribution to the total oxygen loss of the OC. Section 1 (S1), contains data from 0 to 11.11 % X; section 2 (S2), data from 11.11 to 33.33 % X, and section 3 (S3) contains the rest of the data.

In previous studies, the partitioning of the data was done based on the *ln-ln* plot (Eq. (5)) of the overall conversion (Hancock and Sharp, 1972; Zhang et al., 2019, 2017). The *ln-ln* plot of the overall conversion data for the reduction of the OC with CH_4 is shown in Figure 3. Two distinct slopes can be observed on the plot, indicating two governing reaction mechanisms. The inflection point between the two regions corresponds to 33 % overall conversion. No change in the lines' slopes is detected at the point corresponding to 11 % overall conversion, suggesting that the first two reactions are isokinetic. This is revealed by the results of our base model building steps as well (described below). In this work, we propose to partition the data based on the stoichiometric amount of oxygen released by each reaction. This not only aligns well with

the experimental observation but also helps build models able to predict the composition of the OC at any given location inside the reactor as a function of the operating conditions. Having the ability to predict the composition of the OC during operation is advantageous when it comes to process design and operation, as it can be used to determine optimal residence times for different CLC applications relying on the full or partial oxidation of carbonaceous fuels.

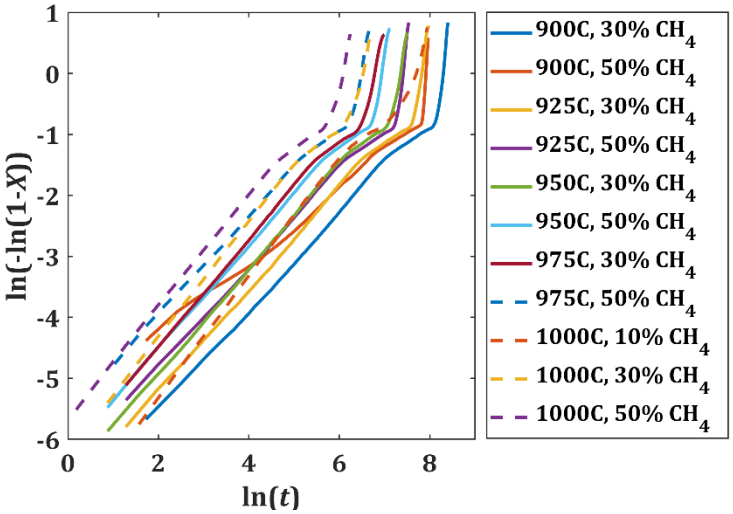

Figure 3. Plot of $\ln[-\ln(1-X)]$ vs. $\ln t$ for the reduction of the OC with CH_4 at different temperatures and gas concentrations.

Following the partitioning of the data, the second step is to map each of the three data sections onto the interval [0, 1]. Then, we proceed to determine the mechanisms and models that best describe each of the data sections using Hancock and Sharp's graphical *ln-ln* method (Hancock and Sharp, 1972). In its simplest form, the Hancock and Sharp *ln-ln* method is based on the following equation to determine the reaction mechanism:

$$\ln[-\ln(1-X)] = \ln B + m \ln t \tag{5}$$

where B [-] is a constant partially dependent on the nucleation frequency and rate of grain growth (therefore, indirectly on the temperature), and m is a constant associated with the geometry of the system. Presentation of the data measured at any given temperature in the specific form of $\ln[-\ln(1-X)]$ vs. $\ln t$ renders straight lines and is indicative of the reaction mechanism via the gradient m: if $m < 1$, the reaction mechanism is most likely a diffusion process, if $1 < m < 2$, the results suggest a phase boundary (or interface) controlled mechanism, whereas if $m > 2$, the nucleation mechanism is most likely dominant (Nasr and Plucknett, 2014). Hancock and Sharp (Hancock and Sharp, 1972) argue that the conversion data used in Eq. (5) should be limited to values from 0.15 to 0.50 to ensure that the data and results are not

affected by uncertainty in the initial conditions, as establishing the zero time for reactions can be difficult. Therefore, in our analysis, after we mapped the conversion onto the [0, 1] interval, we have limited the range of the conversion to values from 0.15 to 0.50 for each of the three data sections. Then we computed the gradient m at every temperature and, using the average values of m and Table 2, identified the mechanism and model that best describe the data in each of the three data sections. It is observed that the gradient m and, therefore, the dominant mechanism does not change with temperature for any of the reaction steps with CH_4 and H_2. However, for the third reaction step in the case of reduction with CO, the gradient m shows a shift in values with temperature, possibly indicating a mechanism shift with increasing temperature. Therefore, for the reduction of the OC with CO, two three-step dynamic models are built and evaluated, with identical mechanisms for the first two reactions, but different mechanisms for the third reaction.

Overall, two reaction mechanisms are predominant: the phase-boundary controlled, contracting volume, or contracting sphere denoted with the letter "C", and the two-dimensional Avrami-Erofe'ev growth of nuclei denoted with the letter "A." The kinetic models identified as most representative of the data, using the base kinetic model development framework presented in this section, are listed in Table 4.

Table 4. Reaction mechanisms and kinetic models for the reduction of the Fe-based OC with CH_4, CO, and H_2.

	CH_4 (CCA)	**CO (ACA/ACC)**	**H_2 (ACC)**
Fe(III) → Fe(II,III)	contracting volume (C)	Avrami-Erofe'ev ($n = 2$) (A)	Avrami-Erofe'ev ($n = 2$) (A)
Fe(II,III) → Fe(II)	contracting volume (C)	contracting volume (C)	contracting volume (C)
Fe(II) → Fe	Avrami-Erofe'ev ($n = 2$) (A)	Avrami-Erofe'ev ($n = 2$) (A) / contracting volume (C)	contracting volume (C)

Furthermore, the kinetic parameters of the models for each reaction step (preexponential factor k_0, energy of activation E_a, and reaction order n) can be estimated via the graphical method detailed in Abad et al. (Abad et al., 2011). The steps to find the kinetic parameters based on the graphical method are described below.

Step A. Determine the time for complete OC conversion, τ_{chr} [s], for each data section by plotting the kinetic model's integral form $g(X)$ as a function of t:

$$g(X) = \frac{1}{\tau_{chr}} t, \qquad \tau_{chr} = \left(bkC_g^n\right)^{-1} \tag{6}$$

Here b [-] is the stoichiometric coefficient for reaction of solid with reacting gas [mol metal oxide per mol of gas], k [mol^{-n} m^{3n} s^{-1}] is the chemical kinetic constant, C_g [mol m^{-3}] is the reactant gas concentration in the TGA, and n [-] is the reaction order.

Step B. Find n and k for every measurement temperature. Eq. (6) can be rewritten as:

$$\ln\left(\frac{1}{b\tau_{chr}}\right) = \ln(k) + n\ln(C_g) \tag{7}$$

For every temperature, plot $\ln\left(\frac{1}{b\tau_{chr}}\right)$ vs. $\ln(C_g)$. This produces linear plots, and n and k values as a function of temperature are obtained by fitting the lines.

Step C. Find k_0 and E_a from the Arrhenius plot. Linearizing Eq. (3) gives:

$$\ln(k) = \ln(k_0) + \left(-\frac{E_a}{R}\right)\frac{1}{T} \tag{8}$$

Plotting $\ln(k)$ as a function of T^{-1} produces a linear curve, and k_0, E_a are obtained from its intercept and slope.

The calculated kinetic parameter values determined via the graphical method are used as initial points for the MCMC algorithm of the Bayesian calibrations. It should be noted that for some calibration runs, these initial points led to a very low acceptance rate of the MCMC sampler and have been changed on a trial-and-error basis.

Having identified the reaction mechanisms and kinetic models that best describe the reduction of the OC with the three fuels, the next step is to formulate the dynamic model that will be the base kinetic model of our Bayesian calibration and model building framework.

Stage II. Dynamic Base Kinetic Model

The base dynamic kinetic models are written in terms of the OC conversion and consist of ordinary differential equations (Eqs. (9a)-(9c)) describing the particle reduction dynamics. The functions f_{R1}, f_{R2}, f_{R3} are the differential rates as listed in Table 2, determined in Part I of our model building framework (given in Table 4). The general forms of the reaction rates of each reaction step are written as:

$$\frac{1}{\tau_{chr_{R1}}}\frac{dX_{R1}}{dt} = f_{R1}(X_{R1}) \tag{9a}$$

$$\frac{1}{\tau_{chr_{R2}}}\frac{dX_{R2}}{dt} = \frac{KI_{R2}}{1 + KI_{R2} - X_{R1}} f_{R2}(X_{R2}) \tag{9b}$$

$$\frac{1}{\tau_{chr_{R3}}}\frac{dX_{R3}}{dt} = \frac{KI_{R3}}{1 + KI_{R3} - X_{R2}} f_{R3}(X_{R3}) \tag{9c}$$

where X_{R1} [-], X_{R2} [-], and X_{R3} [-] are the conversions of the OC for each reaction step, and $KI_{R2}(1 + KI_{R2} - X_{R1})^{-1}$ and $KI_{R3}(1 + KI_{R3} - X_{R2})^{-1}$ are functions that help model the observed

dynamics for CH_4 and CO. These functions are referred to as transitioning functions in the remainder of the paper. As previously described, for carbonaceous fuels the reaction rate is fast before it tapers off as the OC conversion approaches 33 % (see Figures 1 (a)-(c) and 2). As the reaction progresses beyond 33 % conversion, the conversion rate increases again. This behavior suggests that the third reaction starts after the first and second reactions are complete. Furthermore, since the operating conditions at which the reaction mechanisms proceed at a maximum rate may not be the same, the inflection point where the sharp acceleration is observed varies with temperature and gas concentration. The transitioning functions have the unique flexibility to accommodate the shift between the relative importance of the three rate controlling mechanisms, delaying the onset of the second and third reactions as needed, dictated by the experimental data. The KI [-] parameters of the functions are calibration parameters, thus allowing the data to shape their posterior distributions. As shown in Figure 4, the transitioning function's range is 0 to 1, and at very low KI values its output is very close to zero for most of the previous reaction's conversion domain. When the conversion approaches one, there is a sharp increase in the transitioning function's output. For large KI values, the transitioning function's output is close to one for the entire conversion domain, and its effect becomes negligible.

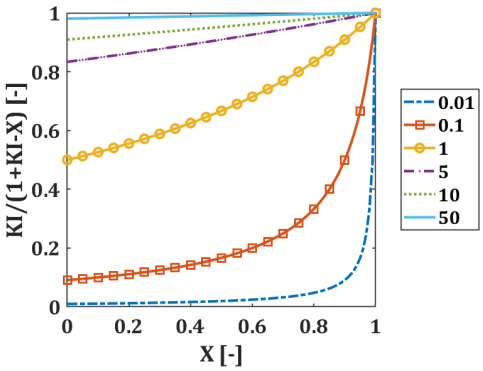

Figure 4. The transitioning function as a function of overall conversion X (x-axis) and KI parameter values (each line corresponds to the KI value listed in the legends).

Thus, putting it all together, the base kinetic model for the reduction of the Fe-based OC with CH_4 is:

$$\frac{dX_{R1}}{dt} = k_{0,R1}\exp\left(\frac{-E_{a,R1}}{RT}\right) b_{R1} C_g^{n_{R1}} 3(1-X_{R1})^{2/3} \tag{10a}$$

$$\frac{dX_{R2}}{dt} = \frac{KI_{R2}}{1+KI_{R2}-X_{R1}} k_{0,R2}\exp\left(\frac{-E_{a,R2}}{RT}\right) b_{R2} C_g^{n_{R2}} 3(1-X_{R2})^{2/3} \tag{10b}$$

$$\frac{dX_{R3}}{dt} = \frac{KI_{R3}}{1+KI_{R3}-X_{R2}} k_{0,R3} exp\left(\frac{-E_{a,R3}}{RT}\right) b_{R3} C_g^{n_{R3}} 2\,(1-X_{R3})[-\ln(1-X_{R3})]^{1/2} \tag{10c}$$

This model will be referred to as CCA, as it consists of the contracting sphere rate laws describing the first two reactions (the first two reactions are isokinetic as indicated by Figure 3), and the two-dimensional Avrami-Erofe'ev describing the third reaction.

Next, for the reduction of the Fe-based OC with CO we have two base kinetic models due to the mechanism shift that was observed in the TGA data as the experimental temperature increases. The ACA, i.e., the two-dimensional Avrami-Erofe'ev rate law describes the first and third reactions, and the contracting sphere describes the second reaction:

$$\frac{dX_{R1}}{dt} = k_{0,R1}\exp\left(\frac{-E_{a,R1}}{RT}\right) b_{R1} C_g^{n_{R1}} 2\,(1-X_{R1})[-\ln(1-X_{R1})]^{1/2} \tag{11a}$$

$$\frac{dX_{R2}}{dt} = \frac{KI_{R2}}{1+KI_{R2}-X_{R1}} k_{0,R2}\exp\left(\frac{-E_{a,R2}}{RT}\right) b_{R2} C_g^{n_{R2}} 3(1-X_{R2})^{2/3} \tag{11b}$$

$$\frac{dX_{R3}}{dt} = \frac{KI_{R3}}{1+KI_{R3}-X_{R2}} k_{0,R3}\exp\left(\frac{-E_{a,R3}}{RT}\right) b_{R3} C_g^{n_{R3}} 2\,(1-X_{R3})[-\ln(1-X_{R3})]^{1/2} \tag{11c}$$

And the ACC, where the two-dimensional Avrami-Erofe'ev rate law is describing the first reaction, and the contracting sphere is describing the second and third reactions:

$$\frac{dX_{R1}}{dt} = k_{0,R1}\exp\left(\frac{-E_{a,R1}}{RT}\right) b_{R1} C_g^{n_{R1}} 2\,(1-X_{R1})[-\ln(1-X_{R1})]^{1/2} \tag{12a}$$

$$\frac{dX_{R2}}{dt} = \frac{KI_{R2}}{1+KI_{R2}-X_{R1}} k_{0,R2}\exp\left(\frac{-E_{a,R2}}{RT}\right) b_{R2} C_g^{n_{R2}} 3(1-X_{R2})^{2/3} \tag{12b}$$

$$\frac{dX_{R3}}{dt} = \frac{KI_{R3}}{1+KI_{R3}-X_{R2}} k_{0,R3}\exp\left(\frac{-E_{a,R3}}{RT}\right) b_{R3} C_g^{n_{R3}} 3(1-X_{R3})^{2/3} \tag{12c}$$

In the case of reduction with CO, the parameter and model structure uncertainty will be quantified using both base case kinetic models, and the best model among the base kinetic models and discrepancy-augmented ACA and ACC models will be selected using the BIC.

The base kinetic model for the reduction of the Fe-based OC with H_2 has an identical model structure with the ACC of reduction with CO (Eqs. (12)).

For each reacting solid-gas pair, the overall conversion is calculated using a linear combination of the conversions of the OC for each reaction step as:

$$X = w_1 X_{R1} + w_2 X_{R2} + w_3 X_{R3} \tag{13}$$

where w_1 is $1/9$, w_2 is $2/9$, and w_3 is $2/3$, respectively. These values reflect the amount of oxygen that can be extracted from the OC: the $Fe_2O_3 \rightarrow Fe_3O_4$ (Fe(III) → Fe(II,III)) step can extract 11 % of the total

oxygen; the $Fe_3O_4 \rightarrow FeO$ (Fe(II,III) → Fe (II)) step can extract 22 % of the total oxygen; and the $FeO \rightarrow Fe$ (Fe (II) → Fe) step can extract the remaining 67 % of the total oxygen.

Equations (10a) through (12c) describe the reduction kinetics on a conversion basis for each oxidation state of the OC. These types of models are excellent for the modeling of isothermal solid-state reactions kinetics experiments such as TGA experiments. However, since the initial OC mass in the system and the formation of new solid phases are not accounted for in these models, their use in process simulation and optimization can lead to generating faulty predictions. Therefore, these models must be reformulated to be suitable for process simulation and optimization. Using the case of reduction with CH_4 as an example, the reaction rate for the first reduction step (Fe_2O_3 to Fe_3O_4) described by Eq. (10a) is rewritten as:

$$r_{R1} = \frac{\rho_0 w_{Fe2O3,0}}{b_{R1} MW_{Fe2O3}} \frac{dX_{R1}}{dt} = \frac{\rho_0 w_{Fe2O3,0}}{b_{R1} MW_{Fe2O3}} k_{0,R1} \exp\left(\frac{-E_{a,R1}}{RT}\right) b_{R1} C_g^{n_{R1}} 3(1 - X_{R1})^{2/3} \quad (14)$$

Here, r_{R1} [mol m^{-3} s^{-1}] is the reaction rate for the first reaction step, ρ_0 [mol m^{-3}] is the OC particle density at time $t = 0$, $w_{Fe2O3,0}$ [-] is the weight fraction of Fe_2O_3 at time $t = 0$, MW_{Fe2O3} [mol kg^{-1}] is the molecular weight of Fe_2O_3, and b_{R1} [mol of metal oxide per mol of gas] is the stoichiometric coefficient for the reaction of Fe_2O_3 with CH_4. Furthermore, as the Fe_2O_3 molar amount ($C_{s,Fe2O3}$ [mol m^{-3}]) in the OC at each moment is:

$$C_{s,Fe2O3} = \frac{\rho_0 w_{Fe2O3,0}}{MW_{Fe2O3}} (1 - X_{R1}) \quad (15)$$

the reaction rate for the reduction of Fe_2O_3 to Fe_3O_4 becomes:

$$r_{R1} = C_{s,Fe2O3} k_{0,R1} \exp\left(\frac{-E_{a,R1}}{RT}\right) C_g^{n_{R1}} 3(1 - X_{R1})^{(-1/3)} \quad (16a)$$

Applying the same procedure, the reaction rates for the reduction of Fe_3O_4 to FeO, and FeO to Fe are rewritten as:

$$r_{R2} = \frac{KI_{R2}}{1 + KI_{R2} - X_{R1}} C_{s,Fe3O4} k_{0,R2} \exp\left(\frac{-E_{a,R2}}{RT}\right) C_g^{n_{R2}} 3(1 - X_{R2})^{(-1/3)} \quad (16b)$$

$$r_{R3} = \frac{KI_{R3}}{1 + KI_{R3} - X_{R2}} C_{s,FeO} k_{0,R3} exp\left(\frac{-E_{a,R3}}{RT}\right) C_g^{n_{R3}} 2\,[-\ln(1 - X_{R3})]^{1/2} \quad (16c)$$

In the case of reduction of the OC with CO, the ACA model becomes:

$$r_{R1} = C_{s,Fe2O3} k_{0,R1} \exp\left(\frac{-E_{a,R1}}{RT}\right) C_g^{n_{R1}} 2\,[-\ln(1 - X_{R1})]^{1/2} \quad (17a)$$

$$r_{R2} = \frac{KI_{R2}}{1 + KI_{R2} - X_{R1}} C_{s,Fe3O4} k_{0,R2} \exp\left(\frac{-E_{a,R2}}{RT}\right) C_g^{n_{R2}} 3(1 - X_{R2})^{(-1/3)} \quad (17b)$$

$$r_{R3} = \frac{KI_{R3}}{1 + KI_{R3} - X_{R2}} C_{s,FeO} k_{0,R3} \exp\left(\frac{-E_{a,R3}}{RT}\right) C_g^{n_{R3}} 2\,[-\ln(1 - X_{R3})]^{1/2} \quad (17c)$$

while the ACC model is rewritten as:

$$r_{R1} = C_{s,Fe2O3} k_{0,R1} \exp\left(\frac{-E_{a,R1}}{RT}\right) C_g^{n_{R1}} 2\,[-\ln(1 - X_{R1})]^{1/2} \quad (18a)$$

$$r_{R2} = \frac{KI_{R2}}{1 + KI_{R2} - X_{R1}} C_{s,Fe3O4} k_{0,R2} \exp\left(\frac{-E_{a,R2}}{RT}\right) C_g^{n_{R2}} 3(1 - X_{R2})^{(-1/3)} \quad (18b)$$

$$r_{R3} = \frac{KI_{R3}}{1 + KI_{R3} - X_{R2}} C_{s,FeO} k_{0,R3} \exp\left(\frac{-E_{a,R3}}{RT}\right) C_g^{n_{R3}} 3(1 - X_{R3})^{(-1/3)} \quad (18c)$$

Since the base kinetic model for the reduction of the OC with H_2 (ACC) has the same model structure as the ACC of reduction with CO, its reformulation is the same as that given by Eqs. (18a)-(18c).

While using the second formulation of the models (Eqs. (16a)-(18c)) is recommended for process simulation and optimization, both modeling formulations are very well suited for use as base models for the Bayesian calibration of the TGA data. However, the second formulation proved to be somewhat stiff when compared to the first formulation (Eqs. (10a)-(12c)). Since the model parameters' posterior distribution is estimated via MCMC sampling entailing the integration of the dynamic kinetic models many ($\mathcal{O}(10^5)$) times, we decided to use the first formulation for calibration to reduce computation time.

To prevent the first formulation of the kinetic models from generating faulty predictions due to its not having the initial mass and the formation of new solid phases incorporated, a set of penalty functions are implemented in the MCMC simulations for the second and third reaction. The penalty functions are of the form:

$$penalty_1 = \max\left(1, \frac{X_{R2}}{X_{R1}}\right)^2 \quad (19a)$$

$$penalty_2 = \max\left(1, \frac{X_{R3}}{X_{R2}}\right)^2 \quad (19b)$$

Using the penalty functions, the overall conversion of the OC (Eq. (5.13)) is rewritten as:

$$X^{new} = X\, penalty_1\, penalty_2 \quad (20)$$

The implemented penalty functions ensure that the second reaction does not reach completion before the first one, and the third does not reach completion before the first or second one.

5 Parameter and Model Structure Uncertainty Quantification

In Bayesian inference, the parameters of the calibrated model are considered to be random variables, thus their estimates are not a single value (point estimates) but a probability density function, which effectively is the measure of the uncertainty of the parameters. A distinct advantage of Bayesian calibration is that the probability distributions of parameters are more informative than point estimates or even interval estimates (e.g., confidence intervals (CIs)) of parameters (Reilly and Blau, 1974). A 95 % CI, for example, implies that if we repeat an experiment 100 times and compute the 95 % CI for all 100 experiments, 95 (95 %) of these CIs would contain the true unknown parameter, while 5 (5%) of these CIs would not contain the true unknown estimate. A common misinterpretation of CIs is that there is, in the case of the 95 % CI, a 95 % probability that the true value of the estimated parameter falls within the CI. This interpretation is incorrect because CIs are computed by treating the estimated parameter as a fixed unknown value and, therefore, this fixed value is either inside or outside the interval with 100% (or 0%) probability (Hespanhol et al., 2019; Sim and Reid, 1999; Tan and Tan, 2010). The essential function of CIs is to examine a characteristic of a sample in terms of its degree of variability in the corresponding population (Sim and Reid, 1999). In contrast, Bayesian inference estimates the most likely values of the parameter of interest directly from the population distribution, and it answers questions about the parameters in a more direct and natural way. The main result of Bayesian calibration is the posterior probability distribution, which can be described by measures of tendency (e.g., median, mean, or mode) and measures of uncertainty (e.g., variance or standard deviation). A measure of uncertainty in Bayesian inference that is analogous to CIs is the Bayesian credible interval. A 95 % Bayesian credible interval or region, for example, conveys that there is a 95 % probability that the true value of the estimated parameter falls within the interval, given the evidence provided by the observed data (Hespanhol et al., 2019; Lesaffre and Lawson, 2012). Furthermore, the Bayesian parameter estimates in the form of posteriors can be interpreted in a probabilistic way, showing that parameter values with higher probability are more plausible than those with lower probability. This information is not available in the statement of either a point estimate or an interval estimate. The main disadvantage of using Bayesian inference for parameter estimation is the complexity of computing posterior distributions, which is why it has not been widely used despite it having been suggested for building models of reaction systems close to fifty years ago (Froment, 1975; Reilly and Blau, 1974). Fortunately, computational advances since then enable the effective implementation and use of Bayesian inference for model building and parameter estimation.

In the following, the fundamental theory and methodology of Bayesian inference are briefly presented, covering the fundamental concepts necessary for the presentation of our uncertainty quantification framework and results. For an extensive description, readers are referred to the collection of papers on

applications of Bayesian methods using MCMC algorithms edited by Gilks, Richardson and Spiegelhalter (Gilks et al., 1995).

5.1 Bayesian Approach for Parameter Estimation

Bayesian calibration starts with a prior distribution $\mathcal{P}(\theta)$ of the parameters θ that reflects our *beliefs* (knowledge) about the values of parameters without taking any of the experimental data into consideration, e.g., some parameters should be positive or should fall within a specific range. Priors are usually established based on experience, literature, and/or preliminary experiments. In this study, the priors of the model parameters are uniform (bounded) and uninformative probability distributions, which allow the data to dominate the estimation of the parameters. The uniform probability distributions are defined as:

$$\mathcal{P}(\theta_i) = \begin{cases} 0 & , \quad \theta_i < \mathrm{LB}_{\theta_i} \\ \dfrac{1}{\mathrm{UB}_{\theta_i} - \mathrm{LB}_{\theta_i}} & , \quad \mathrm{LB}_{\theta_i} < \theta_i < \mathrm{UB}_{\theta_i} \\ 0 & , \quad \mathrm{UB}_{\theta_i} < \theta_i \end{cases} \tag{21}$$

The θ calibration parameters and their lower and upper bounds are given in Table 5.

Table 5. Bounds of the uniform prior probability distributions of the calibration parameters in the base kinetic models.

Parameter	LB	UB
$k_{0,,R1}$ $[\mathrm{mol^{-n}m^{3n}s^{-1}}]$	0.01	26,500,000
$E_{a,\mathrm{R1}}$ $[\mathrm{J\ mol^{-1}}]$	20,000	300,000
$n_{R1}[-]$	0.01	4
$k_{0,,R2}$ $[\mathrm{mol^{-n}m^{3n}s^{-1}}]$	0.01	12,000,000
$E_{a,\mathrm{R2}}$ $[\mathrm{J\ mol^{-1}}]$	50,000	300,000
n_{R2} $[-]$	0.1	3
$k_{0,,R3}$ $[\mathrm{mol^{-n}m^{3n}s^{-1}}]$	0.01	12,000,000
$E_{a,\mathrm{R3}}$ $[\mathrm{J\ mol^{-1}}]$	50,000	300,000
n_{R3} $[-]$	0.1	3
KI_{R2} $[-]$	10^{-5}	200
KI_{R3} $[-]$	6.5×10^{-5}	100

In this work, because the observation error is not known, another prior that needs to be defined is that of the observational error variance, $\mathcal{P}(\psi)$, where ψ is an additional unknown parameter for the calibration. This term acknowledges the existence of error in the experimental measurements, with the experimental uncertainty (uncertainties in the experimental setup and the response variable measurements) being modeled as having a normal distribution with mean 0 and variance ψ, i.e., white noise:

$$\epsilon_i = X_{exp,i} - X_{model,i} \sim N(0, \psi) \tag{22}$$

Here $X_{exp,i}$ is the experimental overall conversion of the OC, and $X_{model,i}$ is the model prediction of the overall conversion of the OC, Eq. (13). The prior distribution chosen for the error variance, $\mathcal{P}(\psi)$, is a diffuse inverse gamma (IG) distribution, a distribution with a strictly positive support. The IG distribution, often used in Bayesian calibration, is the conjugate prior distribution (posterior and prior distributions are from the same family) to a Gaussian white noise likelihood function for fixed θ, allowing for a direct sampling from the conditional posterior for the observational error variance without rejection (Blair and Mebane, 2015; Mejia, 2017). The shape parameters of the IG distribution are chosen such that $\mathcal{P}(\psi)$ is a broad vaguely informative prior, once again allowing the data to shape the posterior of ψ.

The remaining distribution to be defined is the likelihood function, $\mathcal{L}(\mathrm{D}|\theta, \psi)$, which is the "likelihood" that a model with parameters θ reproduces the data D within the error described by Eq. (22) and its parameters ψ. Assuming that the experimental errors $\epsilon_i(\psi)$ (Eq. (22)) for each of the *N* data points are independent and normally distributed random variables with mean zero and variance ψ, the joint probability density function for the *N* data points in the data set D can be written as:

$$\mathcal{L}(\mathrm{D}|\theta, \psi) = \prod_i (2\pi\psi_i)^{-1/2} \exp\left(-\frac{SSE}{2\psi_i}\right) \tag{23}$$

where $SSE = \sum \epsilon_i^2$ is the sum of squared errors. The likelihood of a proposed model and parameters increases as SSE decreases, providing a measure of the goodness of fit to the experimental data. Furthermore, the higher the probability of the proposed model to truly represent the data, the least biased the residuals (Eq. (22)) are, meaning that they are better estimates of the experimental error.

After having defined the prior and likelihood distributions, the next step is to apply Bayes' theorem for parameter estimation. Using Bayes' theorem, the prior is revised using experimental data, D, in the form of the likelihood distribution, and thus the posterior distribution $\Pi(\theta, \psi|\mathrm{D})$ of the parameters is calculated (the data is used to modify (or confirm) the prior belief about the parameters). When applied to the parameter estimation problem, Bayes' theorem is written as:

$$\Pi(\theta, \psi|\mathrm{D}) = \frac{\mathcal{L}(\mathrm{D}|\theta, \psi)\mathcal{P}(\theta)\mathcal{P}(\psi)}{\int_\theta \int_\psi \mathcal{L}(\mathrm{D}|\theta, \psi)\mathcal{P}(\theta)\mathcal{P}(\psi)\mathrm{d}\psi\mathrm{d}\theta} \tag{24}$$

The integral in the denominator is referred to as the marginal likelihood or marginal density of observations, and it is the probability of observing the dataset D over the parameter space of θ and ψ.

The Bayesian approach takes into consideration prior knowledge about both the model parameters and the data measurement error (via the error model used to define the likelihood function), and updates this

knowledge using experimental data. In this way, two main sources of uncertainty—the uncertainty about the true unknown value of model parameters and the experimental error—are addressed. However, there is a third fundamental source of uncertainty that is often overlooked: error in the model structure itself. This model error is the discrepancy between model prediction and the truth, and stems from the deviation of the modeling assumptions from real phenomena. To account for the model error, Kennedy and O'Hagan (Kennedy and O'Hagan, 2001) proposed the inclusion of a discrepancy term in the model itself, writing the statistical model for the data as:

$$d(\xi) = M(\xi, \theta) + \delta(\xi, \beta) + \epsilon(\psi) \tag{25}$$

where d is a stochastic variable representing the experimental data (in our case the overall conversion of the OC), ξ are system conditions (e.g., temperature, partial pressures), M is the model output, δ is the model discrepancy, and β are discrepancy parameters.

5.2 Dynamic Discrepancy

For physical dynamic models, assigning a statistical structure to an additive discrepancy as shown in Eq. (25) is difficult, as there is no associated observable noise structure to justify any specific choice of distribution or correlation structure (Sargsyan et al., 2015). In quantifying model structure uncertainty, the goal of using discrepancy functions is not only to help obtain better parameter estimates, but also to help propagate the uncertainty due to model error to a larger scale system. These goals can be achieved by embedding the model structure discrepancy in the model itself, altering the model structure in a manner that is physically consistent and informative. Using dynamic discrepancy, the essential structure of the base kinetic model can be retained, and Eq. (25) is replaced with a new model for the observed data (Bhat et al., 2017; Lei et al., 2019; Li et al., 2017):

$$d(\xi) = \mathcal{M}\big(\xi, \theta, \delta(\xi, \beta)\big) + \epsilon(\psi) \tag{26}$$

$$\frac{dM}{dt} = F(M, \delta) \tag{27}$$

As the mechanistic base model is a continuous and differentiable model, the discrepancy function is required to be continuous and differentiable as well. To satisfy these requirements, discrepancy functions used are modeled by a GP proposed by Reich et al. (Reich et al., 2009; Storlie et al., 2013). The multivariate discrepancy functions are parameterized using Bayesian Smoothing Spline Analysis of Variance (BSS-ANOVA) and Karhunen-Loéve (KL) decompositions. By using a KL expansion with the BSS-ANOVA GP for modeling the discrepancy, all the stochasticity in the GP is transferred to the β coefficients of δ,

enabling the deterministic evaluation of the likelihood function when β is fixed, and the computational efficiency is drastically increased compared to using a traditional GP. Details of the BSS-ANOVA GP model can be found in Refs. (Bhat et al., 2017; Gu, 2013; Lei et al., 2019; Li et al., 2017; Reich et al., 2009; Storlie et al., 2013). The discrepancy function is, thus, a stochastic process represented as an infinite linear combination of orthogonal functions, and admits a decomposition into main effects, two-way interactions, and higher order interactions:

$$\delta(\xi_i) = \beta_0 + \sum_{i,j} \beta_i^j \phi_j(\xi_i) + \sum_{i,j,k,l} \beta_{ik}^{jl} \phi_j(\xi_i)\, \phi_l(\xi_k) + \cdots \tag{28}$$

where ξ_i is the i-th descriptor of the system state, $\phi_j(\xi_i)$ is the j-th order eigenfunction (scaled by the eigenvalues) in the KL expansion, β_0 is a constant here set to zero (Bhat et al., 2017), and β_i^j (one-way coefficients) and β_{ik}^{jl} (two-way coefficients) are pairwise uncorrelated random variables with independent normal prior distributions centered at 0. Like the error variance, the discrepancy parameters are normally distributed random variables, $\beta \sim \mathcal{N}(0, \tau)$, and the prior distribution chosen for the variance parameters τ is a diffuse IG distribution. The KL eigenfunctions are orthogonal, spectral, non-parametric and ordered, allowing/permitting for the discrepancy function to be written in a systematic way by adding the terms in Eq. (28) into the GPs hierarchically. The infinite expansion can be truncated at some large enough value, as the eigenfunctions have increasingly higher frequency with decreasingly smaller amplitude (Figure 6) and, therefore, the effect of adding terms becomes negligible after a certain number of terms. For most problems, it is sufficient to have only main effects and two-way interactions.

To estimate the parameters of the discrepancy function, they are included in the prior and posterior distributions with the model parameters, and Bayes' theorem (Eq. (24)) is rewritten as:

$$\Pi(\theta, \beta, \tau, \psi|\mathrm{D}) = \frac{\mathcal{L}(\mathrm{D}|\theta, \beta, \psi)\mathcal{P}(\beta|\tau)\mathcal{P}(\theta)\mathcal{P}(\tau)\mathcal{P}(\psi)}{\int_\beta \int_\theta \int_\tau \int_\psi \mathcal{L}(\mathrm{D}|\theta, \beta, \psi)\mathcal{P}(\beta|\tau)\mathcal{P}(\theta)\mathcal{P}(\tau)\mathcal{P}(\psi)\mathrm{d}\psi\mathrm{d}\tau\mathrm{d}\theta\mathrm{d}\beta} \tag{29}$$

The posterior Π is constructed/determined by sampling using the MCMC method, bypassing the computation of the high-dimensional integral (the marginal likelihood) in the denominator of Eq. (29). At each step of the MCMC, a newly proposed set of the parameters θ and β is accepted or rejected based on the Metropolis-Hastings criterion (Hastings, 1970). The τ and ψ variance parameters are updated using a Gibbs sampler (Geman and Geman, 1984). The proposal of the parameters is made as a "block" (Li et al., 2017; Mejia, 2017), allowing the MCMC to take potentially larger steps in the parameter space and decreasing the computational time by reducing the number of kinetic model evaluations/simulations, as each new parameter proposal requires a model evaluation/simulation. A detailed description of the

implementation of the MCMC can be found in Bhat et al. (Bhat et al., 2017).

5.3 Kinetic Models with Dynamic Discrepancy

For the reduction of the Fe-based OC with CH_4, the kinetic model with discrepancy is obtained by rewriting the base kinetic model (Eqs. (10a)-(10c)) as:

$$\frac{dX_{R1}}{dt} = k_{R1}^{new} b_{R1} C_g^{n_{R1}} 3(1 - X_{R1})^{2/3} \tag{30a}$$

$$\frac{dX_{R2}}{dt} = \frac{KI_{R2}^{new}}{1 + KI_{R2}^{new} - X_{R1}} k_{R2}^{\text{new}} b_{R2} C_g^{n_{R2}} 3(1 - X_{R2})^{2/3} \tag{30b}$$

$$\frac{dX_{R3}}{dt} = \frac{KI_{R3}^{\text{new}}}{1 + KI_{R3}^{\text{new}} - X_{R2}} k_{R3}^{new} b_{R3} C_g^{n_{R3}} 2\,(1 - X_{R3})[-\ln(1 - X_{R3})]^{1/2} \tag{30c}$$

$$k_{Ri}^{new} = k_{Ri} \exp\left(\delta_{Ri}(X, T^{-1})\right) = k_{0,Ri} \exp\left(\frac{-E_{a,Ri}}{RT}\right) \exp\left(\delta_{Ri}(X, T^{-1})\right) \tag{30d}$$

$$KI_{Rj}^{new} = KI_{Rj} \exp\left(\delta_{KI_{Rj}}(T, C_g)\right) \tag{30e}$$

The ACA and ACC base models for the reduction of the Fe-based OC with CO and H_2 are rewritten similarly by inserting discrepancy functions in their reaction rate constants and KI transitioning function parameters. In the above equations, $i = \{1,2,3\}$ and $j = \{2,3\}$, and thus five discrepancy functions are used in each model. The discrepancy functions inserted in the reaction rate constants (δ_{Ri}, shown in Eq. (30d)) are a function of the overall OC conversion X and the inverse system temperature T^{-1}. Inserting the discrepancy function in the reaction rate in this manner allows the energy of activation, $E_{a,Ri}$, to vary across the state space, accommodating deviations from ideality where $E_{a,Ri}$ is assumed to be constant. The discrepancy functions inserted in the transitioning functions ($\delta_{KI_{Rj}}$, shown in Eq. (30e)) are a function of system temperature T and reacting gas concentration C_g, allowing the KI parameters to vary with T and C_g, as the transition between the different regions of the overall OC conversion is strongly dependent on the system temperature and reacting gas concentration. The transition is undistinguishable when H_2 is the reacting gas, whereas it is very noticeable when CH_4 is the reacting gas (Figure 1), and it takes place at different time instants depending on the system conditions. The transitioning function is very good at modeling both ends of the observed phenomenology, having an insignificant effect in the model for H_2, and having an inhibitory effect of the third reaction step in the model for CH_4. As mentioned previously, the behavior of the transitioning functions is determined by the KI transitioning function parameters whose values are estimated along with the other model parameters, and by the discrepancy functions whose form and parameters are also determined based on the experimental data.

The explicit Dormand-Prince adaptive time step method (Dormand and Prince, 1980) is used to integrate the dynamic base kinetic and discrepancy-enhanced kinetic models. The method of Dormand and Prince uses a fifth-order Runge-Kutta method to compute each update to the solution and uses a fourth-order Runge-Kutta method to estimate the error.

5.4 Model Selection

The proposed Bayesian model building framework starts with the base kinetic model, followed by the generation of new hybrid kinetic models by inserting the discrepancy function in the base model. The discrepancy function and, coincidentally, the most adequate hybrid kinetic model is built systematically by successively adding a one-way or two-way interaction term at a time. The best fitting kinetic model is selected using the Bayesian Information Criterion (BIC), a measure for Bayesian model comparison introduced by Schwartz (Schwarz, 1978). For each model, the BIC is computed as (Liddle, 2007):

$$\mathrm{BIC} = -2 \ln L_{max} + \Theta \ln N \tag{31}$$

where L_{max} is the maximum value of the likelihood function for the model under consideration, Θ is the number of estimated parameters, and N is the number of observations in the experimental data. The best model is the model with the lowest BIC. Generally, a difference of at least two units between model candidates' BIC scores is considered as positive evidence against the other models (Fabozzi et al., 2014). The use of the BIC guards against overfitting of more complex models by rewarding goodness of fit and penalizing model complexity. In conclusion, the proposed Bayesian model building framework is systematic and computationally tractable, producing a hybrid kinetic model that contains corrections for any model structure inadequacies stemming from modeling assumptions and unknown phenomena, while retaining its mechanistic basis.

6 Results and Discussion

6.1 Final Dynamic Kinetic Model

The best-fitting kinetic model is developed through an iterative procedure that requires multiple model proposals and calibrations. MCMC simulations with 400,000 steps were used to calibrate each of the proposed models, and the last 150,000 steps were used to calculate the BIC statistic. In the first iteration (no discrepancy function), the base kinetic model is calibrated, estimating the posterior of its 11 parameters $\left(\theta = \left\{k_{0,R1}, E_{a,R1}, n_{R1}, k_{0,R2}, E_{a,R2}, n_{R2}, k_{0,R3}, E_{a,R3}, n_{R3}, KI_{R2}, KI_{R3}\right\}\right)$, and its BIC statistic is calculated. In the subsequent iterations, increasingly complex models are proposed by successively including new terms in the discrepancy functions. The terms of each of the five discrepancy functions are

added in the following order: one-way interaction terms of the overall conversions X (in the rate law discrepancy functions) and temperature T (in the transitioning function discrepancy functions), respectively, and two-way interaction terms between X and T^{-1}, and T and reacting gas concentration C_g. The kinetic models with discrepancy functions have the 11 base kinetic model parameters and $5 \times n$ discrepancy model parameters to be estimated, where n equals the number of terms in the discrepancy functions. In each iteration of the Bayesian model development process, the BIC statistic is calculated for each proposed model, and the model with the lowest BIC is selected as the best model. Figures 5 (a), (b), and (c) show the BIC statistic of all models proposed and calibrated in this study. It can be observed that the BIC decreases with the addition of new terms in the discrepancy function until a minimum BIC is reached, followed by increasing BIC values indicating model overfitting.

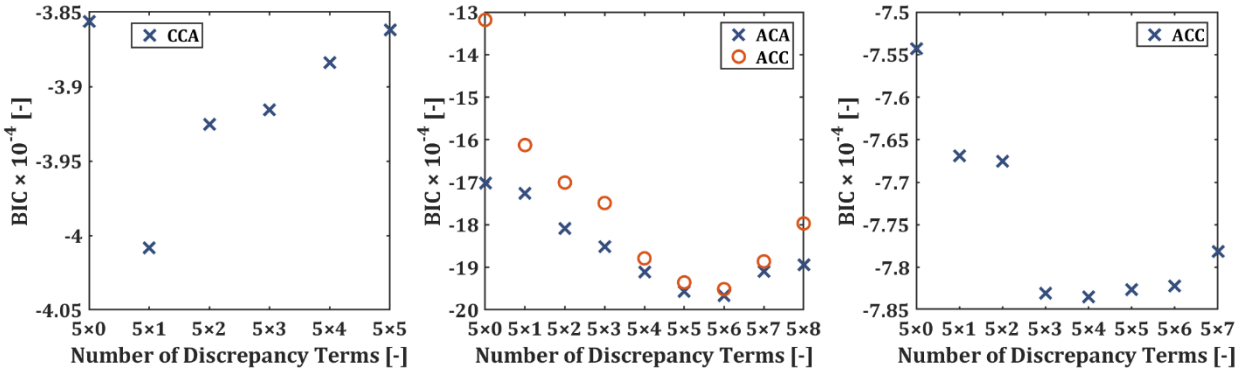

(a) CH_4 **(b)** CO **(c)** H_2

Figure 5. Bayesian Information Criterion (BIC) of the base kinetic models and models with discrepancy functions for the reduction of the OC with **(a)** CH_4, **(b)** CO, and **(c)** H_2.

For the reduction of the OC with CH_4, hybrid models with up to five terms in each discrepancy function were formulated and calibrated. The model with one term in the discrepancy functions has the lowest BIC (Figure 5 (a)), and thus the discrepancy functions with one term inserted in the kinetic rate laws are written using the first eigenfunction in the KL expansion:

$$\delta_{Ri}(X) = \beta_{1,Ri}\phi_1(X) \tag{32a}$$

and the discrepancy functions inserted in the transitioning functions are:

$$\delta_{KI_{Rj}}(T) = \beta_{1,KI_{Rj}}\phi_1(T) \tag{32b}$$

For the reduction of the OC with CO, hybrid models with up to eight terms in each discrepancy function were proposed and calibrated for both ACA and ACC base kinetic models. Figure 5 (b) shows that the ACA model is always better at predicting the experimental data than the ACC model, and that the ACA model with six discrepancy terms is most strongly supported by data. The difference between the BIC of the ACA

and ACC with six discrepancy terms ($\Delta\text{BIC}_6 = \text{BIC}_{6,\text{ACA}} - \text{BIC}_{6,\text{ACC}}$) is 1605.2, which is strong evidence in favor of the ACA model with six discrepancy terms in each discrepancy function (30 terms total). It should be noted that the magnitude of ΔBIC can be interpreted as evidence against a candidate model being the best model, and when $\Delta\text{BIC} > 10$, the evidence is considered to be very strong (Fabozzi et al., 2014). Looking at the within ACA model differences, ΔBIC between the BIC of the ACA model with five and six discrepancy terms (the models with the closest BIC values) is 1096.5, confirming that the ACA model with six terms in its discrepancy functions is most effective in predicting the reduction with CO data. The discrepancy functions with six terms inserted in the kinetic rate laws for the reduction of the OC with CO are written using the first three eigenfunctions in the KL expansion:

$$\begin{aligned}\delta_{Ri}\left(X,\frac{1}{T}\right) = \beta_{1,Ri}\phi_1(X) + \beta_{2,Ri}\phi_1(X)\phi_1\left(\frac{1}{T}\right) + \beta_{3,Ri}\phi_2(X) + \beta_{4,Ri}\phi_2(X)\phi_1\left(\frac{1}{T}\right) \\ + \beta_{5,Ri}\phi_3(X) + \beta_{6,Ri}\phi_3(X)\phi_1\left(\frac{1}{T}\right)\end{aligned} \tag{33a}$$

and the discrepancy functions inserted in the transitioning functions are:

$$\begin{aligned}\delta_{KI_{Rj}}(T, C_g) = \beta_{1,KI_{Rj}}\phi_1(T) + \beta_{2,KI_{Rj}}\phi_1(T)\phi_1(C_g) + \beta_{3,KI_{Rj}}\phi_2(T) \\ + \beta_{4,KI_{Rj}}\phi_2(T)\phi_1(C_g) + \beta_{5,KI_{Rj}}\phi_3(T) + \beta_{6,KI_{Rj}}\phi_3(T)\phi_1(C_g)\end{aligned} \tag{33b}$$

For the reduction of the OC with H_2, models with up to seven discrepancy terms in each discrepancy function were calibrated. The model with four terms in the discrepancy functions (20 terms total) has the lowest BIC (Figure 5 (c)), and ΔBIC between the BIC of the model with three discrepancy terms (having the second lowest BIC) and four discrepancy terms is 46.16, which is strong evidence in favor of the model with four terms. The discrepancy functions with four terms inserted in the kinetic rate laws for the reduction of the OC with H_2 are written using the first two eigenfunctions in the KL expansion:

$$\delta_{Ri}\left(X,\frac{1}{T}\right) = \beta_{1,Ri}\phi_1(X) + \beta_{2,Ri}\phi_1(X)\phi_1\left(\frac{1}{T}\right) + \beta_{3,Ri}\phi_2(X) + \beta_{4,Ri}\phi_2(X)\phi_1\left(\frac{1}{T}\right) \tag{34a}$$

similarly, the discrepancy functions inserted in the transitioning functions are written as:

$$\begin{aligned}\delta_{KI_{Rj}}(T, C_g) = \beta_{1,KI_{Rj}}\phi_1(T) + \beta_{2,KI_{Rj}}\phi_1(T)\phi_1(C_g) + \beta_{3,KI_{Rj}}\phi_2(T) \\ + \beta_{4,KI_{Rj}}\phi_2(T)\phi_1(C_g)\end{aligned} \tag{34b}$$

As mentioned previously, the $\phi_j(\xi)$ eigenfunctions are the eigenfunctions of the KL expansion of the BSS-ANOVA Gaussian process. The first five eigenfunctions are shown in Figure 6. They are defined on the

interval [0,1], and thus the input variables of the discrepancy function need to be mapped onto [0,1]. In this study, since the overall conversion of the OC varies between [0,1] already, only the temperature and inverse temperature are mapped onto [0,1] using a simple linear mapping:

$$\xi(u) = 0.8\frac{u - LB_u}{UB_u - LB_u} - 0.1 \tag{35}$$

where UB_u and LB_u are the upper and lower boundaries of the temperature and inverse temperature, respectively.

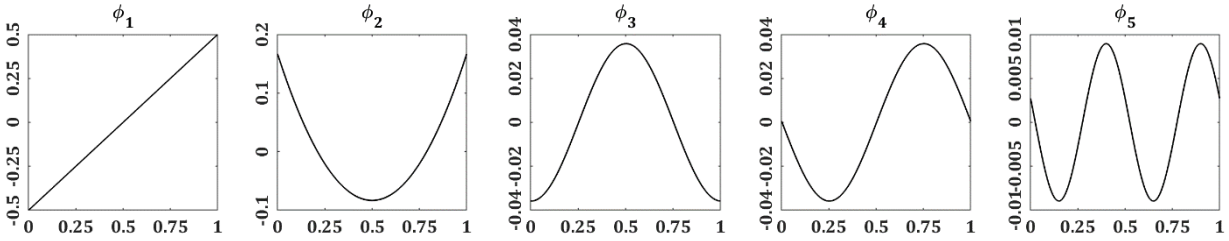

Figure 6. First five eigenfunctions for a main effect from the BSS-ANOVA GP.

As apparent from Eqs. (32a) through (34b), only the first eigenfunction is needed for the prediction of the reduction of the Fe-based OC with CH_4, the first three for the prediction of the reduction of the Fe-based OC with CO, and the first two for the prediction of the reduction of the Fe-based OC with H_2. The eigenfunctions in the discrepancy are not analytical—they are numerically evaluated on a dense grid. To enable the use of the kinetic models with discrepancy in numerical optimization problems, the eigenfunctions are represented as continuous functions: the first eigenfunction is approximated using a first degree polynomial (Eq. (36)), the second eigenfunction is approximated using a seconddegree polynomial (Eq. (37)), while the third eigenfunction is approximated using a sixth degree polynomial (Eq. (38)).

$$\phi_1(\xi) = \xi - 0.5 \tag{36}$$

$$\phi_2(\xi) = \xi^2 - \xi + 0.1667 \tag{37}$$

$$\phi_3(\xi) = -2.185\xi^6 + 6.586\xi^5 - 6.065\xi^4 + 1.107\xi^3 + 0.5517\xi^2 + 0.0055661\xi - 0.03594 \tag{38}$$

The discrepancy functions are, effectively, a measure of the model structure uncertainty inherent in the mechanistic base kinetic models, a measure of the deviations of the mechanistic base model predictions from the real phenomena governing the reduction of the OC. The framework for Bayesian calibration and probabilistic model building presented in this study offers a means for not only quantifying the parameter and model structure uncertainty, but for building the model structure uncertainty quantified in the form of the discrepancy functions into the base mechanistic model. The result is an improved hybrid model consisting of data-driven and mechanistic models that takes into account the deviations of the mechanistic

model's assumptions from reality and provides reliable predictions.

6.2 Parameter Estimates: Posterior Probability and Uncertainty

This section presents the results from the calibration of the three kinetic models selected using the BIC statistic. The results are the posterior distributions of the model parameters, which represent the possible values of the parameters along with a measure of their uncertainty—the probabilities that the model parameters can take the estimated values based on the experimental data. As discussed previously, MCMC methods are used to obtain samples from the posterior distributions of θ, β, and ψ. MCMC simulations with 400,000 steps were used to calibrate each kinetic model. For the OC's reduction with CH_4, convergence to an acceptable posterior probability distribution using MCMC sampling occurred after approximately 150,000 MCMC steps, for reduction with CO after approximately 120,000 steps, and for reduction with H_2 after 210,000 steps. One of the best ways to visualize the posterior is to look at the marginal distributions of the parameters, where we focus our attention on each parameter separately. Figures 7, 8, and 9 show the marginals of θ (the kinetic and transitioning function parameters) for the reduction of the OC with CH_4, CO, and H_2, respectively. The marginals were obtained using kernel smoothing functions that return the probability density estimate of parameters based on the samples obtained from the MCMC simulations.

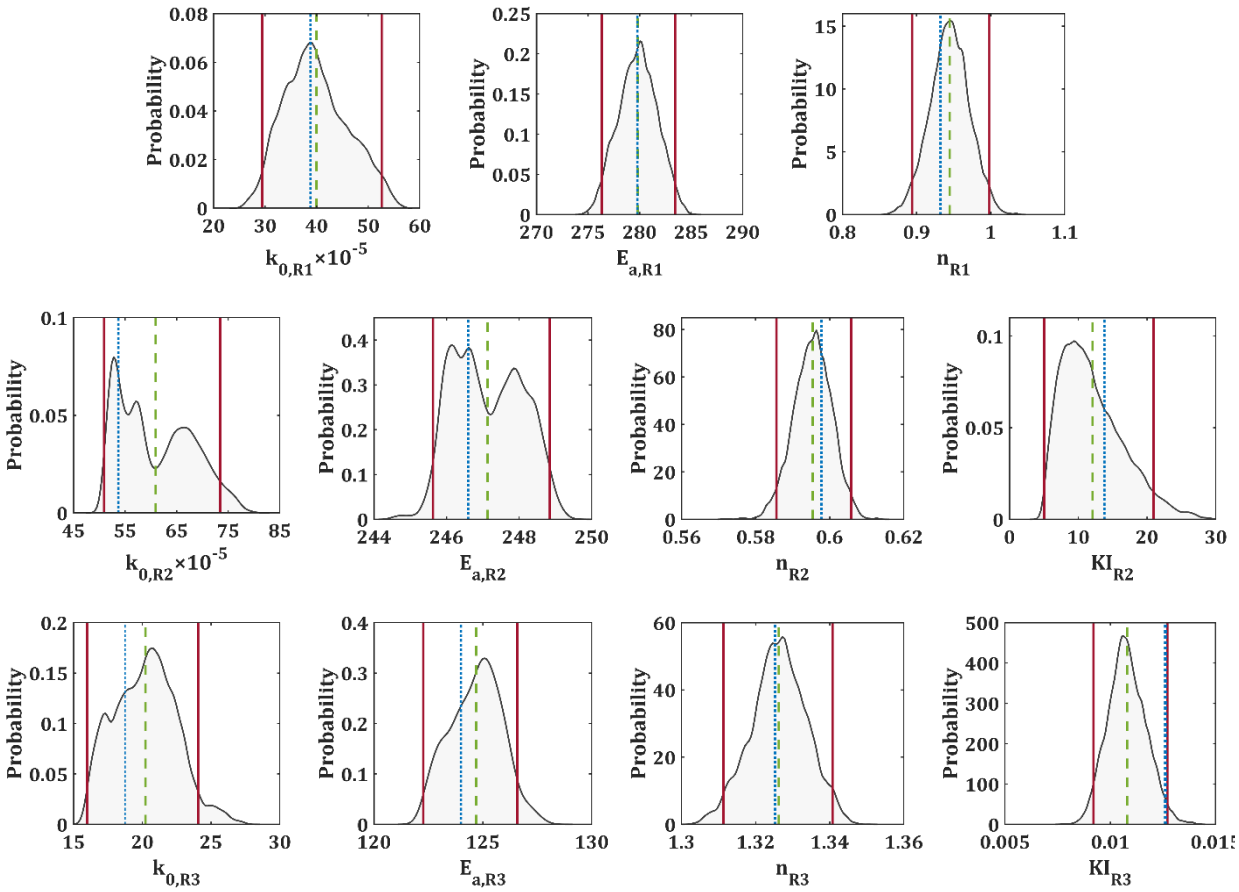

Figure 7. Reduction of the OC with CH_4. Marginal posterior probability density estimates of the parameters of the CCA with discrepancy model.
Vertical continuous red lines indicate the 95 % HDI, dashed green lines indicate the mean, and dotted blue lines indicate the HLPE of the parameters. Discrepancy β parameters are not shown. Units of measurement: $k_{0,,Ri}$ [$\mathrm{mol^{-n}m^{3n}s^{-1}}$], $E_{a,Ri}$ [kJ $\mathrm{mol^{-1}}$], $n_{Ri}[-]$, $KI_{Ri}[-]$.

The marginals reveal the shape of the parameter posterior distributions. Some are symmetrical with a single well-defined peak, such as those of the reaction order parameters for the reduction of the OC with CH_4 and some transitioning function parameters. However, most of the marginal posteriors are highly skewed, which is expected given the nonlinearity of kinetic models (Hsu et al., 2009). Deterministic parameter estimation approaches where model parameters are obtained by minimizing a least squares objective and other statistical methods such as Maximum Likelihood Estimation do not provide this information, as they may not calculate the full probability density functions of model parameters. The information about the uncertainty in the parameters provided by the posteriors, especially when the posteriors are skewed, demonstrates the advantage of Bayesian parameter estimation and uncertainty quantification.

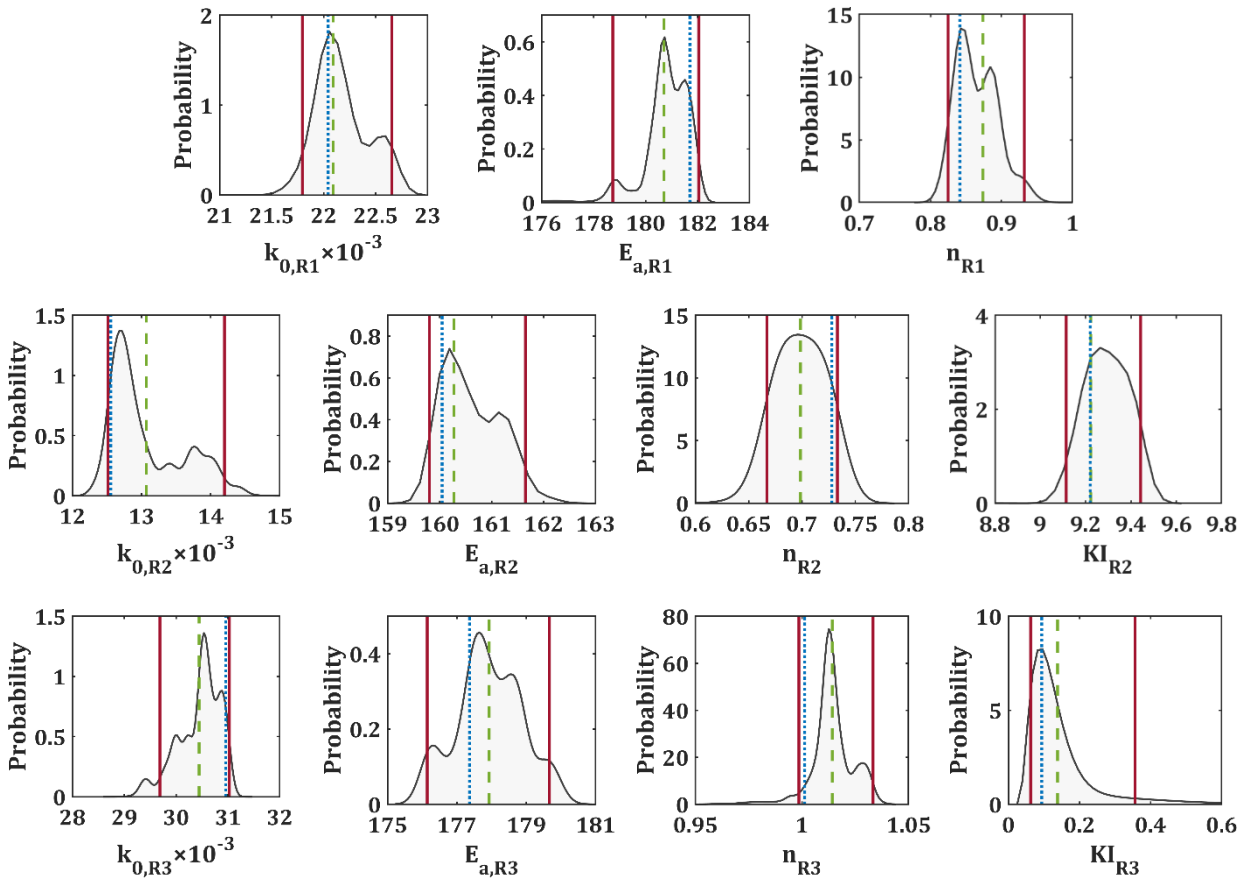

Figure 8. Reduction of the OC with CO. Marginal posterior probability estimates of the parameters of the ACA with discrepancy model. Vertical continuous red lines indicate the 95 % HDI, dashed green lines indicate the mean, and dotted blue lines indicate the HLPE of the parameters. Discrepancy β parameters are not shown.
Units of measurement: $k_{0,,Ri}$ [$\mathrm{mol^{-n}m^{3n}s^{-1}}$], $E_{a,Ri}$ [kJ $\mathrm{mol^{-1}}$], $n_{Ri}[-]$, $KI_{Ri}[-]$.

After obtaining the marginal posteriors, the credible intervals for the parameters are calculated. A commonly used credible interval, the univariate 95 % Highest Density Interval (HDI), is shown on the marginal posterior plots, with the two continuous dark red vertical lines indicating the lower and upper bounds of the interval enclosing 95 % of the parameter space. As per the definition of credible intervals around parameter estimates, given the evidence provided by the observed data, there is a 95 % probability that the true value of the parameters would lie within the obtained intervals. The marginals of each models' parameters have a very narrow distribution and narrow 95 % HDI credible intervals, indicating low uncertainty in the model parameters. Exceptions to this are the preexponential factors $k_{0,R1}$ and $k_{0,R2}$ of the CCA model for the reduction of the OC with CH_4, whose marginal posteriors are quite wide and 95 % HDI quite large.

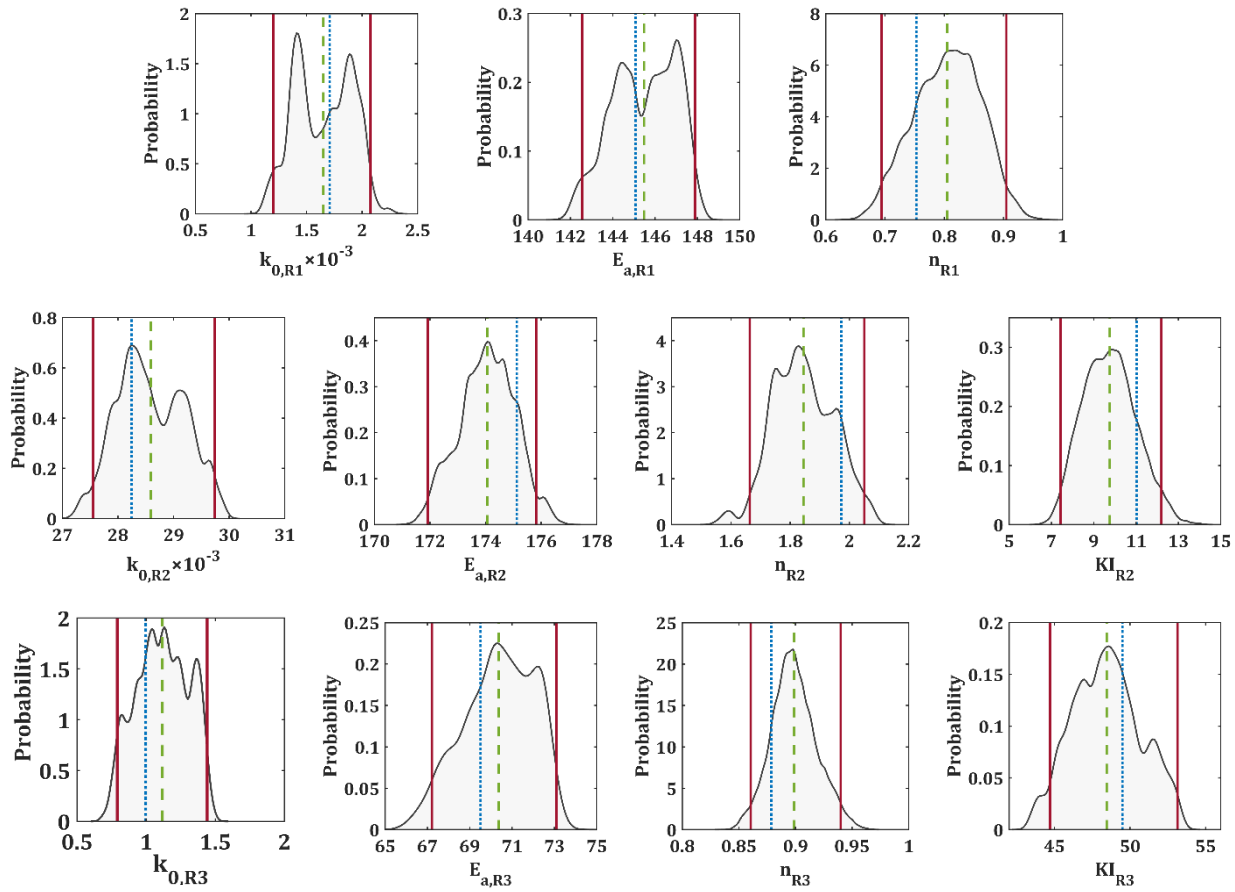

Figure 9. Reduction of the OC with H_2. Marginal posterior probability estimates of the parameters of the ACC with discrepancy model. Vertical continuous red lines indicate the 95 % HDI, dashed green lines indicate the mean, and dotted blue lines indicate the HLPE of the parameters. Discrepancy β parameters are not shown.
Units of measurement: $k_{0,,Ri}$ [$\mathrm{mol^{-n}m^{3n}s^{-1}}$], $E_{a,Ri}$ [$\mathrm{kJ\ mol^{-1}}$], $n_{Ri}[-]$, $KI_{Ri}[-]$.

Furthermore, the mean of the parameters and the parameters corresponding to the highest likelihood—the probability of observing the experimental data given the parameter values, denoted as HLPEs for highest likelihood parameter estimates—are also shown on the plots. The HLPEs rarely coincide with the mean, and even though they are visibly apart on the marginal posterior plots, their values are relatively close given the narrow distributions of the parameters. As the HLPE represents the most probable value for the parameters, it is a reliable choice if a single point estimate needs to be selected.

The discrepancy functions' parameter estimates are not plotted due to space considerations, but lower and upper bounds of their univariate 95 % HDIs, their means, and HLPEs are given in Tables A1, A2, and A3 in the Appendix.

The marginal posteriors are a useful way to visualize the uncertainty of individual model parameters. However, parameters are rarely independent. One way of analyzing the correlation between pairs of model

parameters is using bivariate scatter plots to obtain their joint probability density distributions. Figure 10 shows several bivariate scatter plots of selected parameters of the CCA model (for the reduction of the OC with CH_4). The colors indicate sample density, with yellow representing regions of high sample density and blue representing regions of relatively lower sample density. The shapes of the regions—orientation and elongation—are indicative of the correlation between the parameters. For linear models, the density regions are elliptical, and the correlation between parameters is revealed by the positioning of their axes with respect to the coordinate axes; major/minor axes parallel to the coordinate axes indicate no correlation between parameters (Hsu et al., 2009). As shown in Figure 10, most parameter pairs display low to no correlation. Not surprisingly, strong correlation is observed between preexponential factors $k_{0,Ri}$ and energies of activation $E_{a,Ri}$. While undesirable, these correlations are expected based on the functional form of the Arrhenius equation and have been observed in numerous other studies (Blau et al., 2008; Hsu et al., 2009; Li et al., 2017).

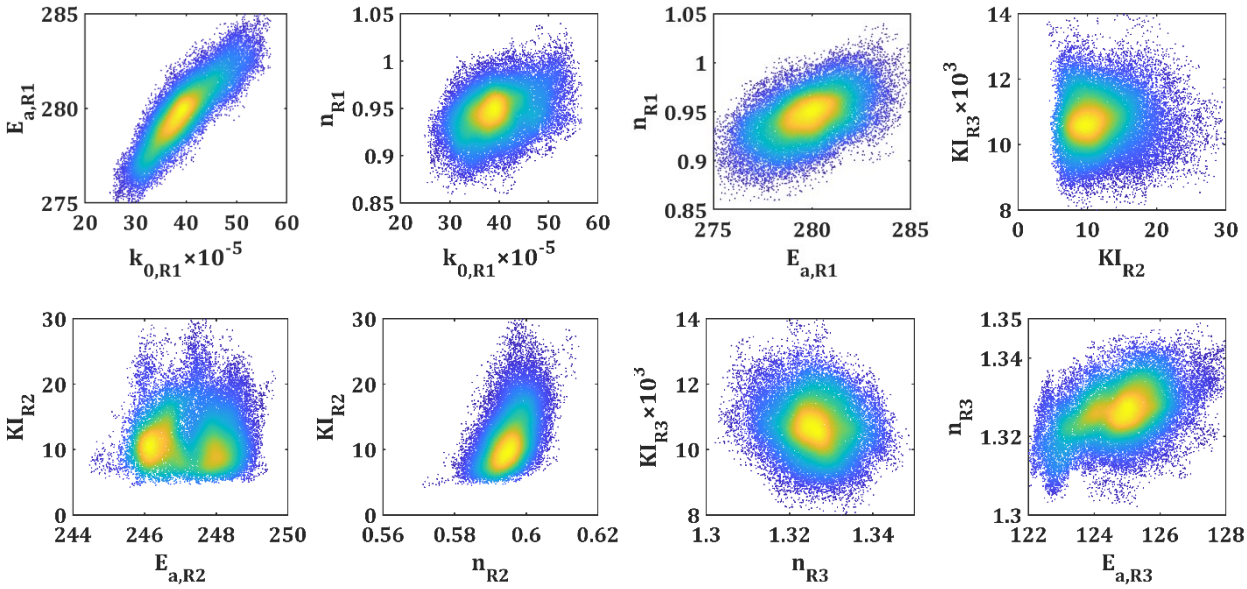

Figure 10. Bivariate scatter plots of selected kinetic and transitioning function parameters of the CCA model. Units of measurement: $k_{0,,Ri}$ [$\mathrm{mol^{-n}m^{3n}s^{-1}}$], $E_{a,Ri}$ [kJ $\mathrm{mol^{-1}}$], $n_{Ri}[-]$, $KI_{Ri}[-]$.

6.3 Kinetic Model Predictions

In this section, the predictions of the selected kinetic models with discrepancy are presented. A sample of size of 150 is drawn from the joint posterior distribution of the model parameters and discrepancy. The corresponding kinetic model predictions are shown in Figure 11 together with the TGA data, showing excellent agreement between model predictions and calibration data. Only two scenarios (data at a certain system conditions) are shown for each reacting solid-gas pair, as the results are very similar for all scenarios. The uncertainty in the predictions is very small, as reflected by the very narrow band formed by the 150

predictions. This is not surprising given the narrow posterior distributions of the model parameters. To help distinguish the 150 predicted conversion curves, insets of zoomed-in regions are provided on each plot. The predictions of the models using the HLPE and mean point estimates of the parameters are also shown for comparison. These, too, are in excellent agreement with the TGA data; however, insets of the distribution of the predicted overall conversion X vs. the conversion computed from the experimental measurements show that the predictions using the HLPEs are closer to the experimental data. Furthermore, the insets of the distribution of the predicted overall conversion (shown at different moments of time) reveal the measure—shape and magnitude—of the uncertainty in the model predictions, which can be readily propagated to a CLC unit/process model for the study of the impact in the kinetic model parameter and model structure uncertainties on larger-scale processes of interest.

An important observation to note is that for the reduction of the OC with CH_4 and CO, the CCA model with one term, and the ACA model with six terms in each of their five discrepancy functions, respectively, accurately predict the OC conversion profiles, and notably, the uptick in the conversion rate after the initial plateau at approximately33 % X. Thus, the developed models with the transitioning functions have the capability to capture and predict the shift between the relative importance of the rate controlling mechanisms governing the reactions. Similarly, the ACC model with four terms in each of its discrepancy functions also accurately predicts the OC conversion profile of the reduction with H_2, in which no inflection point is observed, demonstrating the versatility of the transitioning functions. As described in Section 4, Part II, the transitioning functions are modulated by their KI parameters. Looking at Figure 9, the values of the KI parameters of both transitioning functions of the ACC model are high, with the transitioning functions having an insignificant effect in delaying the onset of the reactions. In contrast, the values of the KI parameters of the CCA (Figure 7) and ACA (Figure 8) models are high for the first transitioning function, but low for the second one. These results suggest that the first and second reaction steps proceed at high rates from the start of the reaction, while the third step is very slow in the beginning, taking off only after the first two steps reach completion.

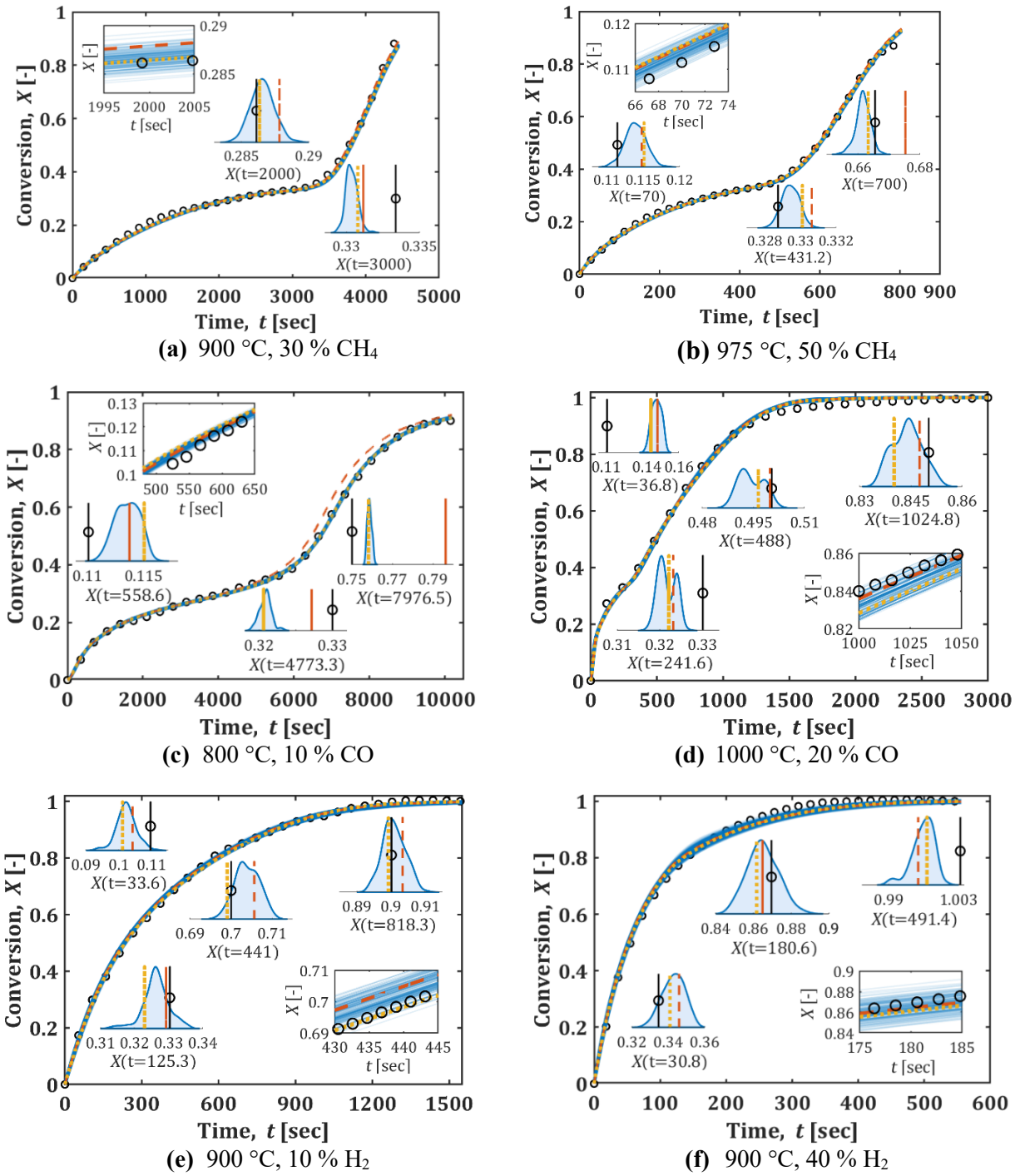

(a) 900 °C, 30 % CH_4 **(b)** 975 °C, 50 % CH_4

(c) 800 °C, 10 % CO **(d)** 1000 °C, 20 % CO

(e) 900 °C, 10 % H_2 **(f)** 900 °C, 40 % H_2

Figure 11. (a)-(b) CCA, **(c)-(d)** ACA, **(e)-(f)** ACC w/ discrepancy model predictions (150 posterior realizations, transparent blue lines) vs. experimental overall conversion (black open circles). Model predictions using mean (dashed orange line) and HLPE (dotted mustard yellow line) point estimates of the parameters are also shown. A zoomed-in inset and insets of the predicted distribution of the overall conversion at fixed times vs. experimental data are provided.

For the reduction of the OC with CH_4, the average root mean square error ($\overline{RMSE}$) and average $\overline{R^2}$

(averaged over the 150 realizations) of the CCA model with one discrepancy term vary between 0.8 and 1.9 %, and 98.99 and 99.86 %, respectively. One exception is the $\overline{RMSE}$ and $\overline{R^2}$ of the 975 °C, 30 % CH_4 scenario, which are outliers at the values of $\overline{RMSE} = 9.39$ % and $\overline{R^2} = 93.9$ %, as the predictions for this scenario are diverging from the experimental data after the 33 % overall conversion mark (Figure 12). A careful inspection of all scenarios' data revealed that the slope of the overall conversion rate after the 33 % overall conversion mark for that scenario is significantly higher than that of the other scenarios, indicating an outlier.

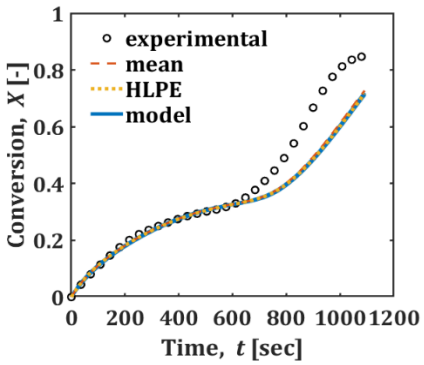

Figure 12. CCA w/ discrepancy model predictions (150 posterior realizations) vs. experimental overall conversion for 975 °C, 30 % CH_4.

For the reduction of the OC with CO, the average root mean square error ($\overline{RMSE}$) and average $\overline{R^2}$ of the ACA model with six discrepancy terms vary between 0.6 and 2.4 %, and 98.76 and 99.95 %, respectively. Similarly, for the reduction of the OC with H_2, the average root mean square error ($\overline{RMSE}$) and average $\overline{R^2}$ of the ACC model with four discrepancy terms vary between 0.6 and 1.9 %, and 98.99 and 99.95 %.

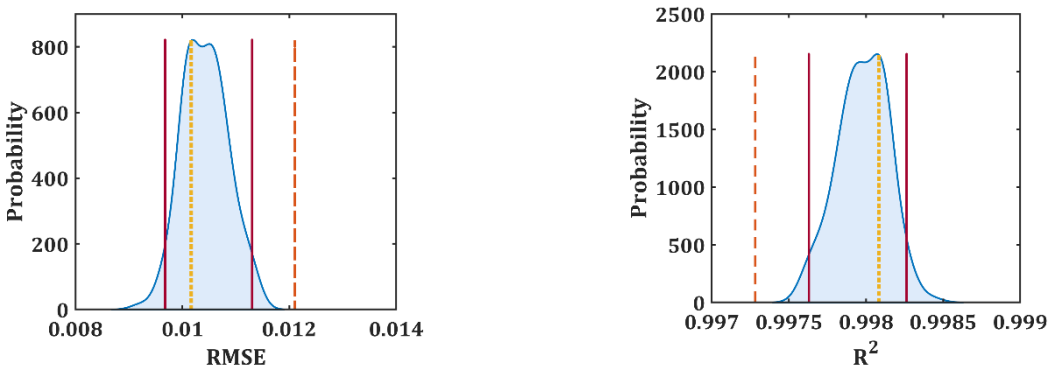

Figure 13. Distribution of $RMSE$ and R^2 values of the CCA model with one discrepancy term for the 975 °C, 50 % CH_4 reduction scenario. Vertical continuous red lines indicate the 95 % HDIs, dashed orange lines indicate the $RMSE$ and R^2 of the prediction using the mean, and dotted mustard yellow lines indicate the $RMSE$ and R^2 of the prediction using the HLPE of the parameters.

As another illustrative example of the uncertainty in the model predictions, Figure 13 shows the distribution of the $RMSE$ and R^2 values of the CCA model with one discrepancy term for the 975 °C, 50 % CH_4 reduction scenario. For this example, the distributions have two peaks, with the $RMSE$ and R^2 values of the prediction with the HLPE of the model parameters coinciding with the highest probability peak, while the $RMSE$ and R^2 values of the prediction with the mean of the model parameters falling outside the 95 % HDI credible intervals.

Selecting a point estimate is controversial in Bayesian statistics. Reporting the HDI confidence limits without specifying a point estimate is strongly preferred (Hsu et al., 2009). However, in practice, selecting a point estimate can be very useful and is generally accepted. Using one of the point estimates reported in this paper (given in Tables A1, A2, and A3 in the Appendix) enables the use of the kinetic models with discrepancies in their predictive capacities in studies where the propagation of uncertainty might not be of interest. For this purpose, the authors recommend using the HLPEs of the model (kinetic, transitioning function and discrepancy) parameters.

6.4 Validation of the Calibrated Model

The predictive capacity of the CCA model with discrepancy is validated by comparing the model predictions to scenarios from a new set of data for the reduction of the OC with CH_4 not used in the parameter estimation process. Predictions using the sample of size 150 from the joint posterior distribution pf parameters are shown in Figure 14 together with the TGA data set aside for validation. The model predictions are in very good agreement with the data of the scenarios that fall within the experimental conditions of the calibration data (Figures 14 (c) and (e)). Furthermore, the agreement is also very good for the three scenarios where temperature and gas concentration are extrapolated (Figures 14 (a), (b), and (d)).

The average $\overline{RMSE}$ and average $\overline{R^2}$ of the CCA model with one discrepancy term vary between 0.76 and 7.98 %, and 84 and 99.27 %, respectively.

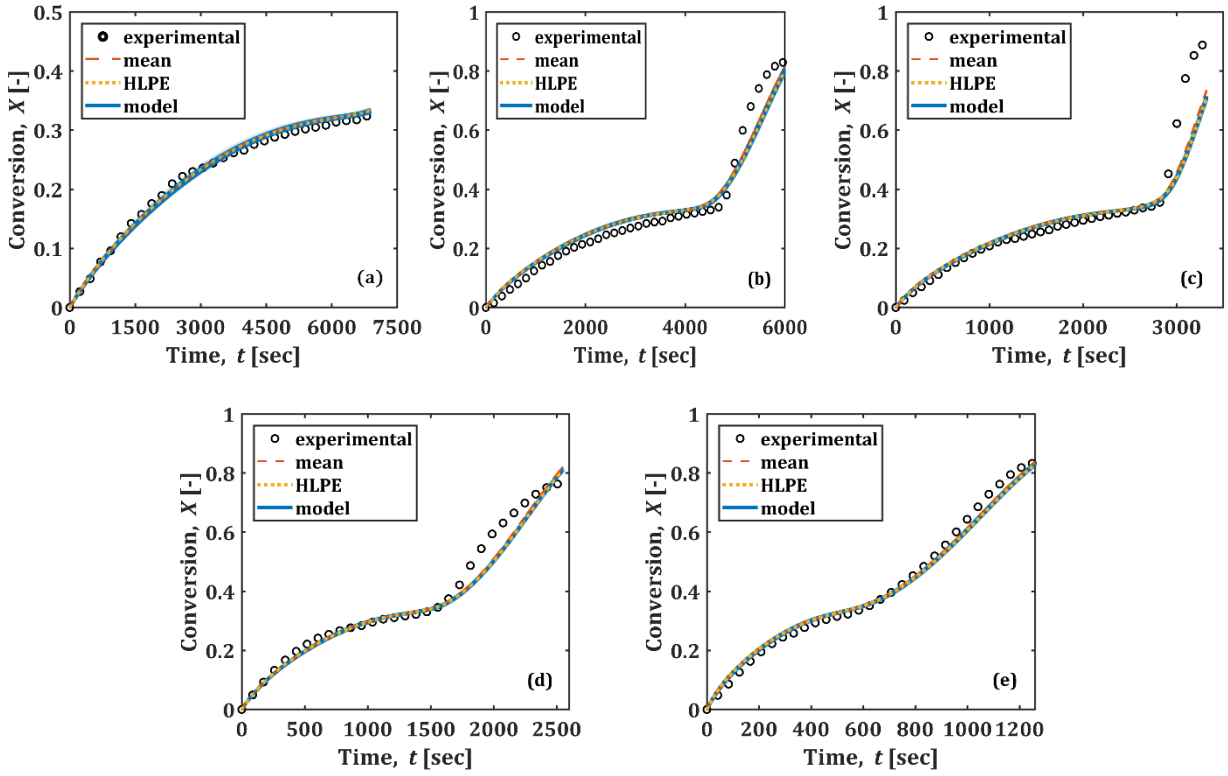

Figure 14. CCA w/ discrepancy model predictions (150 posterior realizations, transparent blue lines) vs. experimental overall conversion (black open circles) for **(a)** 900 °C, 10 % CH_4, **(b)** 900 °C, 20 % CH_4, **(c)** 900 °C, 40 % CH_4, **(d)** 950 °C, 20 % CH_4, **(e)** 1000 °C, 20 % CH_4. Model predictions using mean (dashed orange line) and HLPE (dotted mustard yellow line) point estimates of the parameters also shown.

These results show that the model is reliable and accurate not only within the bounds of the operating conditions of the data used for parameter estimation and model structure uncertainty quantification, but also outside those bounds.

7 Conclusions

A Bayesian model building and parameter estimation framework for CLC systems has been presented in this paper. The Bayesian framework was applied to the multi-step complete reduction of an Fe-based OC with the most often encountered gaseous fuels: CH_4, CO, and H_2. Dynamic kinetic models with BSS-ANOVA dynamic discrepancy functions were built for the complete reduction of the OC, and their parameters were estimated, quantifying the uncertainty in model parameters and model structure

simultaneously in the form of the full posterior probability distribution of the parameters. A set of transitioning functions was used to help model the complex dynamics seen in the conversion curves of the OC reduction. The transitioning functions proved to have the capability to aid the kinetic models in fitting very different particle reduction dynamics using the same base model structure. Model predictions are in excellent agreement with experimental data across the entire range of experimental conditions.

The kinetic models with BSS-ANOVA dynamic discrepancy functions have the benefit of being compatible with equation-oriented modeling and optimization frameworks, thus enabling the propagation of the kinetic uncertainty to a unit/process model of interest. The operating conditions at the unit/process scale may be different than those under which the TGA data used to build and calibrate the models were measured, and thus caution should be exercised when using the kinetic models to limit extrapolation as much as possible. However, note that this approach for quantifying the model structure and parameter uncertainty accounts for some extrapolation uncertainty, as demonstrated in the case of the reduction of the OC with CH_4 by a very good agreement between the discrepancy-enhanced kinetic model predictions and a new set of TGA data that has not been used for calibration.

The models used in the Bayesian calibrations are independent of the initial OC mass in the system, and the formation of new solid phases is not accounted for in these models, as they are formulated on a conversion basis. This formulation, however, has very short solution times, making them excellent model candidates for use in Bayesian calibration as they have to be integrated at every iteration of the parameter search algorithm. However, when coupled with a unit/process model, the model predictions have to be related to the initial OC mass in the system, as well as to the formation of new solid phases. We have provided the formulation of the kinetic models that reflects this, writing the models in a form ready for use in process simulation and optimization problems.

The kinetic models with discrepancy are not only suitable for propagating the uncertainty inherent to the TGA model, but upon the selection of appropriate point estimates. They can also be used in deterministic equation-oriented optimization and control applications that rely on numerical solvers, as the models with discrepancy are twice continuously differentiable. The lower and upper bounds of the 95 % HDI credible interval of the kinetic, transitioning function, and discrepancy function parameters, along with the parameters corresponding to the HLPE, and the mean of the parameters are provided in Tables A1, A2, and A3 in the Appendix. As the HLPE represents the most probable value for the parameters, it is an appropriate choice for a point estimate to allow the use of the models simply in their predictive capacity for applications where the propagation of uncertainty might not be of primary interest. Finally, we note that the use of the posterior sample is preferred from a Bayesian perspective, as it conveys significantly more information about uncertainty than parameter point estimates with confidence intervals.

Acknowledgements

This effort is part of the U.S. Department of Energy's Institute for the Design of Advanced Energy Systems (IDAES) supported by the Office of Fossil Energy's Crosscutting Research Program. The authors would like to acknowledge funding from the U.S. Department of Energy's National Energy Technology Laboratory under the Mission Execution and Strategic Analysis contract (DE-FE0025912) for support services.

Appendix

The mean, HLPE, lower and upper bounds of the 95 % HDI credible interval of the kinetic, transitioning function, and discrepancy function parameters are given in the tables below for the dynamic kinetic models of the reduction of the Fe-based OC with CH_4 (Table A1), CO (Table A2), and H_2 (Table A3).

Table A1. Point estimates and 95 % HDI lower and upper bounds of the CCA model with one discrepancy term in each of its five discrepancy functions.

Parameter	Mean	HLPE	95% LB	95% UB
$k_{0,,R1}$ [$\mathrm{mol^{-n}m^{3n}s^{-1}}$]	3994965.00	3883281.82	2946387.00	5262222.00
$k_{0,,R2}$ [$\mathrm{mol^{-n}m^{3n}s^{-1}}$]	6094415.00	5369286.24	5094260.00	7344003.00
$k_{0,,R3}$ [$\mathrm{mol^{-n}m^{3n}s^{-1}}$]	20.2309	18.71	15.9800	24.0600
$E_{a,\mathrm{R1}}$ [$\mathrm{J\ mol^{-1}}$]	279824.10	279776.00	276309.00	283431.00
$E_{a,\mathrm{R2}}$ [$\mathrm{J\ mol^{-1}}$]	247132.70	246592.00	245623.00	248847.00
$E_{a,\mathrm{R3}}$ [$\mathrm{J\ mol^{-1}}$]	124686.00	123992.00	122263.00	126576.00
$n_{R1}[-]$	0.9446	0.9322	0.8939	0.9979
$n_{R2}[-]$	0.5954	0.5978	0.5856	0.6058
$n_{R3}[-]$	1.3263	1.3253	1.3113	1.3408
KI_{R2} [−]	12.096120	13.793000	5.040900	20.930200
KI_{R3} [−]	0.010790	0.012609	0.009200	0.012700
$\beta_{1,R1}$ [−]	-6.6247	-6.7367	-7.2787	-6.0071
$\beta_{1,R2}$ [−]	2.9508	2.7317	2.5055	3.3731
$\beta_{1,R3}$ [−]	0.8629	0.8974	0.7098	1.0050
$\beta_{1,KI_{R2}}$ [−]	-0.7680	-0.5387	-2.0849	0.4669
$\beta_{1,KI_{R3}}$ [−]	2.8301	2.7320	2.5951	3.0680

Table A2. Point estimates and 95 % HDI lower and upper bounds of the ACA model with six discrepancy term in each of its six discrepancy functions.

Parameter	Mean	HLPE	95% LB	95% UB
$k_{0,,R1}$ [$\mathrm{mol^{-n}m^{3n}s^{-1}}$]	22092.56	22044.00	21795.10	22656.20
$k_{0,,R2}$ [$\mathrm{mol^{-n}m^{3n}s^{-1}}$]	13070.26	12556.70	12515.40	14199.90
$k_{0,,R3}$ [$\mathrm{mol^{-n}m^{3n}s^{-1}}$]	30444.93	30956.20	29687.90	31028.80
$E_{a,\mathrm{R1}}$ [$\mathrm{J\ mol^{-1}}$]	180706.10	181700.00	178738.00	182038.00
$E_{a,\mathrm{R2}}$ [$\mathrm{J\ mol^{-1}}$]	160277.00	160048.00	159806.00	161649.00
$E_{a,\mathrm{R3}}$ [$\mathrm{J\ mol^{-1}}$]	177929.60	177361.00	176142.00	179668.00
$n_{R1}[-]$	0.8737	0.8414	0.8247	0.9320
$n_{R2}[-]$	0.6986	0.7280	0.6672	0.7332
$n_{R3}[-]$	1.0142	1.0013	0.9985	1.0333

KI_{R2} [−]	9.222777	9.220790	9.114400	9.442400
KI_{R3} [−]	0.138242	0.093912	0.062400	0.356700
$\beta_{1,R1}$ [−]	-7.2696	-7.6164	-7.6215	-6.7310
$\beta_{2,R1}$ [−]	-2.1368	-2.2719	-2.4285	-1.8130
$\beta_{3,R1}$ [−]	-5.2383	-5.4014	-5.4885	-4.9380
$\beta_{4,R1}$ [−]	8.8817	9.0116	8.5126	9.2248
$\beta_{5,R1}$ [−]	-9.7365	-9.6258	-9.9747	-9.4697
$\beta_{6,R1}$ [−]	14.7029	13.2049	13.1688	14.8900
$\beta_{1,R2}$ [−]	2.3288	2.3542	2.0230	2.3542
$\beta_{2,R2}$ [−]	-3.2770	-3.3924	-3.4586	-3.2188
$\beta_{3,R2}$ [−]	6.4439	5.8007	5.6874	6.9334
$\beta_{4,R2}$ [−]	14.3263	14.8059	14.0586	14.8346
$\beta_{5,R2}$ [−]	-15.8783	-15.7392	-16.0216	-15.7302
$\beta_{6,R2}$ [−]	-11.3358	-12.7404	-12.8196	-8.7101
$\beta_{1,R3}$ [−]	1.5942	1.3396	0.9969	2.2984
$\beta_{2,R3}$ [−]	8.2103	8.1367	8.1001	8.3654
$\beta_{3,R3}$ [−]	-3.7266	-3.5764	-4.0718	-3.3516
$\beta_{4,R3}$ [−]	-23.5554	-24.9796	-27.3543	-19.1032
$\beta_{5,R3}$ [−]	12.2160	11.7691	11.3769	13.0547
$\beta_{6,R3}$ [−]	36.7350	37.0754	35.2782	38.1680
$\beta_{1,KI_{R2}}$ [−]	9.1680	9.3015	9.0078	9.4169
$\beta_{2,KI_{R2}}$ [−]	-10.5401	-10.4794	-10.9094	-10.4036
$\beta_{3,KI_{R2}}$ [−]	1.8901	1.7924	1.7522	1.9949
$\beta_{4,KI_{R2}}$ [−]	-7.6324	-8.0935	-8.3842	-6.9228
$\beta_{5,KI_{R2}}$ [−]	-2.8445	-2.7509	-3.2882	-2.5756
$\beta_{6,KI_{R2}}$ [−]	45.5776	45.9394	45.0422	46.7138
$\beta_{1,KI_{R3}}$ [−]	0.4601	0.6943	-0.0451	0.8952
$\beta_{2,KI_{R3}}$ [−]	11.6785	11.4195	11.2751	11.9991
$\beta_{3,KI_{R3}}$ [−]	-13.3606	-13.2223	-13.5595	-12.9535
$\beta_{4,KI_{R3}}$ [−]	9.6587	9.5921	9.5277	9.9475
$\beta_{5,KI_{R3}}$ [−]	-4.8866	-4.8784	-5.0793	-4.8296
$\beta_{5,KI_{R3}}$ [−]	31.6975	32.3265	30.0419	32.7582

Table A3. Point estimates and 95 % HDI lower and upper bounds of the ACC model with one discrepancy term in each of its four discrepancy functions.

Parameter	Mean	HLPE	95% LB	95% UB
$k_{0,,R1}$ [$\mathrm{mol^{-n}m^{3n}s^{-1}}$]	1652.00	1708.35	1201.51	2074.60
$k_{0,,R2}$ [$\mathrm{mol^{-n}m^{3n}s^{-1}}$]	28587.83	28243.60	27555.20	29742.80
$k_{0,,R3}$ [$\mathrm{mol^{-n}m^{3n}s^{-1}}$]	1.12	1.00	0.79	1.44

$E_{a,\mathrm{R1}}$ [J mol^{-1}]	145474.60	145071	142562.00	147886.00
$E_{a,\mathrm{R2}}$ [J mol^{-1}]	174063.90	175120	171930.00	175817.00
$E_{a,\mathrm{R3}}$ [J mol^{-1}]	70364.80	69513.30	67210.70	73094.20
$n_{R1}[-]$	0.8051	0.7528	0.6943	0.9046
$n_{R2}[-]$	1.8444	1.9727	1.6638	2.0504
$n_{R3}[-]$	0.8989	0.8786	0.8605	0.9400
KI_{R2} [−]	9.757816	11.0184	7.429400	12.196500
KI_{R3} [−]	48.453670	49.4928	44.715300	53.137700
$\beta_{1,R1}$ [−]	-1.4417	-1.0953	-1.8994	-1.0202
$\beta_{2,R1}$ [−]	8.9730	8.1794	7.7320	10.0450
$\beta_{3,R1}$ [−]	4.0986	2.6094	1.3207	7.1259
$\beta_{4,R1}$ [−]	-3.1711	-1.8198	-6.5748	-0.5200
$\beta_{1,R2}$ [−]	1.5832	1.6166	0.8860	2.2353
$\beta_{2,R2}$ [−]	8.5153	8.1474	7.0650	10.0852
$\beta_{3,R2}$ [−]	3.2650	4.0745	1.6226	5.2572
$\beta_{4,R2}$ [−]	-18.5571	-16.2183	-19.9998	-16.1032
$\beta_{1,R3}$ [−]	-1.7704	-1.8254	-1.9115	-1.6292
$\beta_{2,R3}$ [−]	3.9597	3.8994	3.3296	4.5389
$\beta_{3,R3}$ [−]	-2.3781	-2.6099	-3.1966	-1.6233
$\beta_{4,R3}$ [−]	-4.7505	-4.4773	-6.0660	-3.5697
$\beta_{1,KI_{R2}}$ [−]	-2.3933	-2.1551	-3.4761	-1.4127
$\beta_{2,KI_{R2}}$ [−]	-17.4271	-16.4307	-18.7697	-15.8960
$\beta_{3,KI_{R2}}$ [−]	-16.6457	-17.6681	-18.5606	-14.4084
$\beta_{4,KI_{R2}}$ [−]	-2.8537	-3.9961	-6.5955	1.0236
$\beta_{1,KI_{R3}}$ [−]	-11.9737	-11.9399	-13.4283	-10.7476
$\beta_{2,KI_{R3}}$ [−]	5.1644	5.0888	3.4940	6.8172
$\beta_{3,KI_{R3}}$ [−]	3.1354	5.5406	-3.1110	7.2274
$\beta_{4,KI_{R3}}$ [−]	-13.3810	-12.1151	-17.1777	-10.6875

References

Abad, A., Adánez, J., Cuadrat, A., García-Labiano, F., Gayán, P., de Diego, L.F., 2011. Kinetics of redox reactions of ilmenite for chemical-looping combustion. Chem. Eng. Sci. 66, 689–702. https://doi.org/10.1016/J.CES.2010.11.010

Abad, A., Adánez, J., García-Labiano, F., de Diego, L.F., Gayán, P., Celaya, J., 2007a. Mapping of the range of operational conditions for Cu-, Fe-, and Ni-based oxygen carriers in chemical-looping combustion. Chem. Eng. Sci. 62, 533–549. https://doi.org/10.1016/J.CES.2006.09.019

Abad, A., García-Labiano, F., de Diego, L.F., Gayán, P., Adánez, J., 2007b. Reduction kinetics of Cu-, Ni-, and Fe-based oxygen carriers using syngas (CO + H2) for chemical-looping combustion. Energy and Fuels 21, 1843–1853. https://doi.org/10.1021/ef070025k

Adánez, J., De Diego, L.F., García-Labiano, F., Gayán, P., Abad, A., Palacios, J.M., 2004. Selection of oxygen carriers for chemical-looping combustion. Energy and Fuels 18, 371–377. https://doi.org/10.1021/ef0301452

Bhat, K.S., Mebane, D.S., Mahapatra, P., Storlie, C.B., 2017. Upscaling Uncertainty with Dynamic Discrepancy for a Multi-Scale Carbon Capture System. J. Am. Stat. Assoc. 112, 1453–1467. https://doi.org/10.1080/01621459.2017.1295863

Blair, J., Mebane, D.S., 2015. A Bayesian approach to electrical conductivity relaxation and isotope exchange/secondary ion mass spectrometry. Solid State Ionics 270, 47–53. https://doi.org/10.1016/j.ssi.2014.12.009

Blau, G., Lasinski, M., Orcun, S., Hsu, S.H., Caruthers, J., Delgass, N., Venkatasubramanian, V., 2008. High fidelity mathematical model building with experimental data: A Bayesian approach. Comput. Chem. Eng. 32, 971–989. https://doi.org/10.1016/j.compchemeng.2007.04.008

Campos, D.C., Belkouch, J., Hazi, M., Ould-Dris, A., 2013. Reactivity Investigation on Iron-Titanium Oxides for a Moving Bed Chemical Looping Combustion Implementation. Adv. Chem. Eng. Sci. 3, 47–56. https://doi.org/10.4236/aces.2013.31005

Chen, Y.Y., Nadgouda, S., Shah, V., Fan, L.S., Tong, A., 2020. Oxidation kinetic modelling of Fe-based oxygen carriers for chemical looping applications: Impact of the topochemical effect. Appl. Energy 279, 115701. https://doi.org/10.1016/j.apenergy.2020.115701

Cheng, Z., Qin, L., Fan, J.A., Fan, L.S., 2018. New Insight into the Development of Oxygen Carrier Materials for Chemical Looping Systems. Engineering. https://doi.org/10.1016/j.eng.2018.05.002

Dormand, J.R., Prince, P.J., 1980. A family of embedded Runge-Kutta formulae. J. Comput. Appl. Math. 6, 19–26. https://doi.org/10.1016/0771-050X(80)90013-3

Fabozzi, F.J., Focardi, S.M., Rachev, S.T., Arshanapalli, B.G., 2014. The Basics of Financial Econometrics: Tools, Concepts, and Asset Management Applications. John Wiley & Sons, Inc., Hoboken, NJ, USA. https://doi.org/10.1002/9781118856406

Froment, G.F., 1975. Model discrimination and parameter estimation in heterogeneous catalysis. AIChE J. 21, 1041–1057. https://doi.org/10.1002/aic.690210602

García-Labiano, F., de Diego, L.F., Adánez, J., Abad, A., Gayán, P., 2004. Reduction and Oxidation Kinetics of a Copper-Based Oxygen Carrier Prepared by Impregnation for Chemical-Looping

Combustion. https://doi.org/10.1021/IE0493311

Geman, S., Geman, D., 1984. Stochastic Relaxation, Gibbs Distributions, and the Bayesian Restoration of Images. IEEE Trans. Pattern Anal. Mach. Intell. PAMI-6, 721–741. https://doi.org/10.1109/TPAMI.1984.4767596

Gilks, W.R., Richardson, S., Spiegelhalter, D. (Eds.), 1995. Markov Chain Monte Carlo in Practice, 1st ed. Chapman and Hall/CRC.

Gu, C., 2013. Smoothing Spline ANOVA Models, Springer Series in Statistics. Springer New York, New York, NY. https://doi.org/10.1007/978-1-4614-5369-7

Han, L., 2016. Dynamic Simulation, Optimization, and Control of Flexible Chemical-Looping Combustion Processes. University of Connecticut.

Han, L., Zhou, Z., Bollas, G.M., 2014. Heterogeneous modeling of chemical-looping combustion. Part 2: Particle model. Chem. Eng. Sci. 113, 116–128. https://doi.org/10.1016/j.ces.2014.03.030

Hancock, J.D., Sharp, J.H., 1972. Method of Comparing Solid-State Kinetic Data and Its Application to the Decomposition of Kaolinite, Brucite, and BaCO3. J. Am. Ceram. Soc. 55, 74–77. https://doi.org/10.1111/j.1151-2916.1972.tb11213.x

Hastings, W.K., 1970. Monte Carlo Sampling Methods Using Markov Chains and Their Applications. Biometrika 57, 97. https://doi.org/10.2307/2334940

Hespanhol, L., Vallio, C.S., Costa, L.M., Saragiotto, B.T., 2019. Understanding and interpreting confidence and credible intervals around effect estimates. Brazilian J. Phys. Ther. 23, 290–301. https://doi.org/10.1016/j.bjpt.2018.12.006

Hsieh, T.L., Xu, D., Zhang, Y., Nadgouda, S., Wang, D., Chung, C., Pottimurphy, Y., Guo, M., Chen, Y.Y., Xu, M., He, P., Fan, L.S., Tong, A., 2018. 250 kWth high pressure pilot demonstration of the syngas chemical looping system for high purity H2 production with CO2 capture. Appl. Energy 230, 1660–1672. https://doi.org/10.1016/j.apenergy.2018.09.104

Hsu, S.-H., Stamatis, S.D., Caruthers, J.M., Delgass, W.N., Venkatasubramanian, V., Blau, G.E., Lasinski, M., Orcun, S., 2009. Bayesian Framework for Building Kinetic Models of Catalytic Systems. Ind. Eng. Chem. Res. 48, 4768–4790. https://doi.org/10.1021/ie801651y

Kathe, M. V., Empfield, A., Na, J., Blair, E., Fan, L.-S., 2016. Hydrogen production from natural gas using an iron-based chemical looping technology: Thermodynamic simulations and process system analysis. Appl. Energy 165, 183–201. https://doi.org/10.1016/J.APENERGY.2015.11.047

Kennedy, M.C., O'Hagan, A., 2001. Bayesian calibration of computer models. J. R. Stat. Soc. Ser. B (Statistical Methodol. 63, 425–464. https://doi.org/10.1111/1467-9868.00294

Khawam, A., Flanagan, D.R., 2006. Solid-State Kinetic Models: Basics and Mathematical Fundamentals. J. Phys. Chem. B 110, 17315–17328. https://doi.org/10.1021/jp062746a

Lee, A., Ghouse, J.H., Eslick, J.C., Laird, C.D., Siirola, J.D., Zamarripa, M.A., Gunter, D., Shinn, J.H., Dowling, A.W., Bhattacharyya, D., Biegler, L.T., Burgard, A.P., Miller, D.C., 2021. The IDAES Process Modeling Framework and Model Library – Flexibility for Process Simulation and Optimization. J. Adv. Manuf. Process.

Lei, Y., Cheng, T. Le, Mebane, D.S., Wen, Y.H., 2019. Reduced-order model for microstructure

evolution prediction in the electrodes of solid oxide fuel cell with dynamic discrepancy reduced modeling. J. Power Sources 416, 37–49. https://doi.org/10.1016/j.jpowsour.2019.01.046

Lesaffre, E., Lawson, A.B., 2012. Bayesian Biostatistics, 1st ed. Wiley.

Lewis, W.K., Gilliland, E.R., 1954. Production of pure carbon dioxide. 195,262.

Li, K., Mahapatra, P., Bhat, K.S., Miller, D.C., Mebane, D.S., 2017. Multi-scale modeling of an amine sorbent fluidized bed adsorber with dynamic discrepancy reduced modeling. React. Chem. Eng. 2, 550–560. https://doi.org/10.1039/C7RE00040E

Liddle, A.R., 2007. Information criteria for astrophysical model selection.

Luo, M., Wang, S., Wang, L., Lv, M., 2014. Reduction kinetics of iron-based oxygen carriers using methane for chemical-looping combustion. J. Power Sources 270, 434–440. https://doi.org/10.1016/j.jpowsour.2014.07.100

Mejia, A., 2017. Study of Parameter Estimation and Model Calibration Using Bayesian Analysis of Noisy Data for a Virus Model. Grad. Theses, Diss. Probl. Reports. West Virginia University Libraries. https://doi.org/10.33915/etd.6211

Miller, D.C., Agarwal, D.A., Tong, C., Sun, X., Tong, C., 2011. CCSI and the role of advanced computing in accelerating the commercial deployment of carbon capture systems. SciDAC 2011 Conf.

Miller, D.D., Siriwardane, R., 2013. Mechanism of methane chemical looping combustion with hematite promoted with CeO2, in: Energy and Fuels. American Chemical Society, pp. 4087–4096. https://doi.org/10.1021/ef302132e

Nadgouda, S.G., Kathe, M. V., Fan, L.S., 2017. Cold gas efficiency enhancement in a chemical looping combustion system using staged H2 separation approach. Int. J. Hydrogen Energy 42, 4751–4763. https://doi.org/10.1016/j.ijhydene.2016.12.005

Nasr, S., Plucknett, K.P., 2014. Kinetics of Iron Ore Reduction by Methane for Chemical Looping Combustion. Energy & Fuels 28, 1387–1395. https://doi.org/10.1021/ef402142q

Ostace, A., Kocan, K.X., Mebane, D.S., Schmal, J.P., Bhattacharyya, D., 2019. Probabilistic Model Building with Uncertainty Quantification and Propagation for a Dynamic Fixed Bed CO2 Capture Process. Energy and Fuels 34, 2516–2532. https://doi.org/10.1021/acs.energyfuels.9b03250

Park, C., Hsieh, T.L., Pottimurthy, Y., Shah, V., Xu, D., Chen, Y.Y., Fan, L.S., Tong, A., 2020. Design and Operations of a 15 kWth Subpilot Unit for the Methane-to-Syngas Chemical Looping Process with CO2 Utilization. Ind. Eng. Chem. Res. 59, 6886–6899. https://doi.org/10.1021/acs.iecr.9b05577

Reich, B.J., Storlie, C.B., Bondell, H.D., 2009. Variable selection in Bayesian smoothing spline ANOVA models: Application to deterministic computer codes. Technometrics 51, 110–120. https://doi.org/10.1198/TECH.2009.0013

Reilly, P.M., Blau, G.E., 1974. The use of statistical methods to build mathematical models of chemical reacting systems. Can. J. Chem. Eng. 52, 289–299. https://doi.org/10.1002/cjce.5450520301

Sargsyan, K., Najm, H.N., Ghanem, R., 2015. On the statistical calibration of physical models. Int. J. Chem. Kinet. 47, 246–276. https://doi.org/10.1002/kin.20906

Schwarz, G., 1978. Estimating the Dimension of a Model. Ann. Stat. 6, 461–464. https://doi.org/10.1214/aos/1176344136

Sim, J., Reid, N., 1999. Statistical Inference by Confidence Intervals: Issues of Interpretation and Utilization. Phys. Ther. 79, 186–195. https://doi.org/10.1093/ptj/79.2.186

Sridhar, D., Tong, A., Kim, H., Zeng, L., Li, F., Fan, L.-S., 2012. Syngas Chemical Looping Process: Design and Construction of a 25 kW $_{th}$ Subpilot Unit. Energy & Fuels 26, 2292–2302. https://doi.org/10.1021/ef202039y

Storlie, C.B., Fugate, M.L., Higdon, D.M., Huzurbazar, A. V., Francois, E.G., McHugh, D.C., 2013. Methods for Characterizing and Comparing Populations of Shock Wave Curves. Technometrics 55, 436–449. https://doi.org/10.1080/00401706.2013.805662

Su, M., Ma, J., Tian, X., Zhao, H., 2017. Reduction kinetics of hematite as oxygen carrier in chemical looping combustion. Fuel Process. Technol. 155, 160–167. https://doi.org/10.1016/j.fuproc.2016.05.015

Syamlal, M., Guenther, C., Cugini, A., Ge, W., Wang, W., Yang, N., Li, J., 2011. Computational science: Enabling technology development. Chem. Eng. Prog. 107, 23–29.

Tan, S.H., Tan, S.B., 2010. The Correct Interpretation of Confidence Intervals. Proc. Singapore Healthc. 19, 276–278. https://doi.org/10.1177/201010581001900316

Tong, A., Bayham, S., Kathe, M. V., Zeng, L., Luo, S., Fan, L.S., 2014. Iron-based syngas chemical looping process and coal-direct chemical looping process development at Ohio State University. Appl. Energy. https://doi.org/10.1016/j.apenergy.2013.05.024

Tong, A., Kathe, M. V., Wang, D., Fan, L.-S., 2018. The Moving Bed Fuel Reactor Process, in: Handbook of Chemical Looping Technology. Wiley-VCH Verlag GmbH & Co. KGaA, Weinheim, Germany, pp. 1–40. https://doi.org/10.1002/9783527809332.ch1

Tong, A., Zeng, L., Kathe, M. V., Sridhar, D., Fan, L.-S., 2013. Application of the Moving-Bed Chemical Looping Process for High Methane Conversion. Energy & Fuels 27, 4119–4128. https://doi.org/10.1021/ef3020475

Tong, X., Bowman, W.J., Mejia-Giraldo, A., Crozier, P.A., Mebane, D.S., 2020. New data-driven interacting-defect model describing nanoscopic grain boundary compositions in ceramics. J. Phys. Chem. C 124, 23619–23625. https://doi.org/10.1021/acs.jpcc.0c05713

Yu, Z., Yang, Y., Yang, S., Zhang, Q., Zhao, J., Fang, Y., Hao, X., Guan, G., 2019. Iron-based oxygen carriers in chemical looping conversions: A review. Carbon Resour. Convers. 2, 23–34. https://doi.org/10.1016/j.crcon.2018.11.004

Zhang, Y. yi, Lü, W., Lü, X. wei, Li, S. ping, Bai, C. guang, Song, B., Han, K. xi, 2017. Isothermal reduction kinetics of Panzhihua ilmenite concentrate under 30vol% CO–70vol% N2 atmosphere. Int. J. Miner. Metall. Mater. 24, 240–248. https://doi.org/10.1007/s12613-017-1401-x

Zhang, Y., Zhao, J., Ma, X., Li, M., Lv, Y., Gao, X., 2019. Isothermal Reduction Kinetics and Mechanism of Pre-oxidized Ilmenite. Mining, Metall. Explor. 36, 825–837. https://doi.org/10.1007/s42461-019-0075-5

Zhang, Z., Yao, J.G., Boot-Handford, M.E., Fennell, P.S., 2018. Pressurised chemical-looping

combustion of an iron-based oxygen carrier: Reduction kinetic measurements and modelling. Fuel Process. Technol. 171, 205–214. https://doi.org/10.1016/j.fuproc.2017.11.018